Hubble Space Telescope spectra of the type Ia supernova SN 2011fe: a tail of low-density, high-velocity material with $Z < Z_\odot$.

P. A. Mazzali[1,2,3] $\star$, M. Sullivan[4], S. Hachinger[2,5], R. S. Ellis[6], P. E. Nugent[7,8],
D. A. Howell[9,10], A. Gal-Yam[11], K. Maguire[12], J. Cooke[13], R. Thomas[8], K. Nomoto[14],
E. S. Walker[15]

[1]*Astrophysics Research Institute, Liverpool John Moores University, IC2, Liverpool Science Park, 146 Brownlow Hill, Liverpool L3 5RF, UK*
[2]*Istituto Nazionale di Astrofisica-OAPd, vicolo dell'Osservatorio 5, 35122 Padova, Italy*
[3]*Max-Planck-Institut für Astrophysik, Karl-Schwarzschild-Str. 1, D-85748 Garching, Germany*
[4]*School of Physics and Astronomy, University of Southampton, Southampton, SO17 1BJ, UK*
[5]*Institut für Theoretische Physik und Astrophysik, Universität Würzburg, Emil-Fischer-Str. 31, 97074 Würzburg, Germany*
[6]*Cahill Center for Astrophysics, California Institute of Technology, Pasadena, CA 91125, USA*
[7]*Department of Astronomy, University of California, Berkeley, CA 94720-3411, USA*
[8]*Computational Cosmology Center, Lawrence Berkeley National Laboratory, 1 Cyclotron Road, Berkeley, CA 94720, USA*
[9]*Las Cumbres Observatory Global Telescope Network, Goleta, CA 93117, USA*
[10]*Department of Physics, University of California, Santa Barbara, CA 93106-9530, USA*
[11]*Benoziyo Center for Astrophysics, Weizmann Institute of Science, 76100 Rehovot, Israel*
[12]*Department of Physics (Astrophysics), University of Oxford, Keble Road, Oxford OX1 3RH*
[13]*Centre for Astrophysics & Supercomputing, Swinburne University of Technology, Mail H30, PO Box 218, Hawthorn, Victoria 3122, Australia*
[14]*Kavli IPMU, University of Tokyo, Kashiwanoha 5-1-5, Kashiwa, Chiba 277-8583, Japan*
[15]*Yale University, Department of Physics, P.O. box 208120, New Haven, CT 06520-8120, USA*

ABSTRACT

Hubble Space Telescope spectroscopic observations of the nearby type Ia supernova (SN Ia) SN 2011fe, taken on 10 epochs from -13.1 to $+40.8$ days relative to B-band maximum light, and spanning the far-ultraviolet (UV) to the near-infrared (IR) are presented. This spectroscopic coverage makes SN 2011fe the best-studied local SN Ia to date. SN 2011fe is a typical moderately-luminous SN Ia with no evidence for dust extinction. Its near-UV spectral properties are representative of a larger sample of local events (Maguire et al. 2012). The near-UV to optical spectra of SN 2011fe are modelled with a Monte Carlo radiative transfer code using the technique of 'abundance tomography', constraining the density structure and the abundance stratification in the SN ejecta. SN 2011fe was a relatively weak explosion, with moderate Fe-group yields. The density structures of the classical model W7 and of a delayed detonation model were tested. Both have shortcomings. An ad-hoc density distribution was developed which yields improved fits and is characterised by a high-velocity tail, which is absent in W7. However, this tail contains less mass than delayed detonation models. This improved model has a lower energy than one-dimensional explosion models matching typical SNe Ia (e.g. W7, WDD1, Iwamoto et al. 1999). The derived Fe abundance in the outermost layer is consistent with the metallicity at the SN explosion site in M101 ($\sim 0.5Z_\odot$). The spectroscopic rise time ($\sim 19\,\mathrm{days}$) is significantly longer than that measured from the early optical light curve, implying a 'dark phase' of ~ 1 day. A longer rise time has significant implications when deducing the properties of the white dwarf and binary system from the early photometric behaviour.

Key words: supernovae: general – supernovae: individual (SN 2011fe) – techniques: spectroscopic – radiative transfer

1 INTRODUCTION

Type Ia supernovae (SNe Ia) remain a well-exploited cosmological probe and an immediate route to understanding the nature of dark

energy (e.g. Riess et al. 1998; Perlmutter et al. 1999; Riess et al. 2007; Kessler et al. 2009; Sullivan et al. 2011; Suzuki et al. 2012). However, the exact nature of the progenitor system is still not well understood, with various astrophysical systematics potentially affecting cosmological measurements (for summaries, see Conley et al. 2011; Howell 2011; Astier 2012). A particularly important systematic is the role of the metallicity, or composition, of the exploding white dwarf star on the outcome of the explosion and the properties of SNe Ia.

It has long been known that the ultraviolet (UV) region of SN Ia spectra effectively traces compositional or metallicity effects (Hoeflich et al. 1998; Lentz et al. 2000). Although the physics underlying the formation of SN Ia UV spectra is complex, the UV is probably the best diagnostic of iron-group element abundances in the outer layers of the SN ejecta (Mazzali 2000; Walker et al. 2012; Hachinger et al. 2013) which are transparent to optical photons. This is closely connected to the density profile of the SN ejecta, and hence to the SN explosion model – the iron-group content of incompletely burned zones is one of the main differences between SN Ia explosions at different metallicity (Iwamoto et al. 1999).

However, data in the UV were historically difficult to obtain. Space observatories are required to perform the observations, and the intrinsic faintness of SNe Ia below ~2700Å requires targets to be relatively nearby to obtain a useful signal-to-noise (S/N). The *International Ultraviolet Explorer* (*IUE*) and the *Hubble Space Telescope* (*HST*) have both been used (Branch & Venkatakrishna 1986; Jeffery et al. 1992; Kirshner et al. 1993; Cappellaro et al. 1995; Sauer et al. 2008a), but generally the data suffer from poor S/N, with only one well-observed SN Ia near maximum light (SN 1992A; Kirshner et al. 1993) and only a few events with early pre-maximum light coverage (e.g. SN 1990N; Leibundgut et al. 1991). A full compilation of observations up to 2004 can be found in Foley et al. (2008b). More recently, the Advanced Camera for Surveys on *HST* observed four SNe Ia (Wang et al. 2012), but the spectral resolution was low making a detailed study difficult.

Some of these earlier difficulties have been alleviated in modern SN searches, which can provide a significant number of early SN Ia events. The Lick Observatory Supernova Search early discovery of SN 2009ig (Foley et al. 2012c) allowed a reasonably high-S/N UV spectral time series to be obtained using *Swift*, and the fast response of that satellite has also allowed spectral series of several other events, although the S/N below 2700Å is not high (Bufano et al. 2009). *HST*, with its larger aperture, has obtained more spectra with a higher S/N, including high-S/N observations of the relatively fast-declining SN 2011iv (Foley et al. 2012b), although these did not commence until maximum light.

A different approach is to focus on the near-UV region down to $\simeq 2900$ Å, which is more easily accessible. At high redshift this wavelength range is redshifted into the optical (e.g. Ellis et al. 2008), and a significant sample of single maximum-light near-UV spectra is now available (Ellis et al. 2008; Foley et al. 2008a; Balland et al. 2009; Foley et al. 2012a). In *HST* cycle 17, we successfully obtained single-epoch near-UV spectra of ~30 lower redshift ($z < 0.08$) SNe Ia at phases close to maximum light (Maguire et al. 2012, hereafter M12), for the most part using early discoveries from the Palomar Transient Factory (PTF; Rau et al. 2009; Law et al. 2009).

M12 presented evidence for evolution in the mean near-UV continuum between $z = 0$ and $z \sim 0.5$, the latter using spectra from Ellis et al. (2008). They demonstrated an excess near-UV flux at ~ 0.5 compared to $z = 0$ at $\simeq 3\sigma$, and showed that this was qualitatively consistent with expected evolutionary effects

due to changes in metallicity via a comparison to SN Ia models (Walker et al. 2012). Even stronger near-UV spectral evolution in the same sense as M12 was presented by Foley et al. (2012a), but over a narrower range in redshift, comparing a ground-based $z \simeq 0$ spectrum and a mean spectrum at $z \sim 0.2$. This would then imply a puzzlingly inconsistent evolution between $z = 0.2$ and $z = 0.5$ – although Foley et al. (2012a) caution that selection effects in the $z \sim 0.2$ sample may play a role in this discrepancy.

In cycle 18, we extended the M12 programme to obtain multi-epoch *HST* SN Ia spectra of four events, from the earliest possible epoch to post-maximum light. Our first spectral series, of SN 2010jn, and its detailed analysis using a radiative transfer code are published in Hachinger et al. (2013). SN 2010jn was an energetic SN Ia explosion, with high expansion velocities and significant amounts of iron-group elements in the outer layers of the ejecta, leading to a high opacity consistent with its slow light curve evolution. Interestingly, the detailed spectral modelling of this event implied a 'rise-time' (the time from SN explosion to maximum light in the B-band) longer than that measured from the optical light curve by ~ 1 day. This suggests the existence of a 'dark phase' between the SN explosion and the emergence of the first photons (Piro & Nakar 2013a,b), in turn implying that the bulk of the radioactive heating from ^{56}Ni, which powers the light curve, must lie deep in the ejecta.

In this paper we present *HST* observations of the second event in our cycle 18 programme, the nearby SN Ia SN 2011fe (Nugent et al. 2011), located in M101. Thanks to the proximity of M101 ($\simeq 6.4$ Mpc, $\mu = 29.04 \pm 0.19$; Shappee & Stanek 2011), SN 2011fe was the brightest SN Ia in the night sky in the 'CCD era', and a comprehensive monitoring campaign carried out across a broad range of wavelengths will make it the best-ever studied SN Ia. Our *HST* data range from the far-UV to the near-infrared (IR), beginning just 4 days after detection and covering 10 epochs. We supplement these *HST* data with spectra taken as part of the PTF follow-up campaign (Parrent et al. 2012). We use a well-established Monte Carlo code (e.g., Lucy 1999; Mazzali 2000; Sauer et al. 2008b; Hachinger et al. 2013) to model this time series of UV/optical spectra. Starting from the outermost regions, we infer the abundance stratification of SN 2011fe, developing a density profile that yields a good fit to the spectra from the UV to the near infrared (IR). We also determine the rise time of the SN from the modelling to compare with the very early SN photometry.

An outline of the paper is as follows. In Section 2 we describe the *HST* observations and their data reduction, and discuss SN 2011fe in the context of other SNe Ia in Section 3. We then introduce the methods used to model the spectra in Section 4, and present the models themselves in Section 5 together with our rise time measurement. We compute spectra for two standard explosion models and for a custom-made density structure which yields improved fits to the spectra. The implications of our results are discussed in Section 6 and we conclude in Section 7.

2 OBSERVATIONS

SN 2011fe was discovered on 2011 August 24.167 (UT) by the PTF using the Palomar 48-in telescope (P48) in M101, at a magnitude of $g \simeq 17.4$ (Nugent et al. 2011, hereafter N11). Within a few hours of discovery, the SN was confirmed as a very early SN Ia using robotic observations with FRODOSPEC on the Liverpool Telescope (LT; Steele et al. 2004). UV/optical/IR spectroscopic observations were subsequently obtained on 10 epochs with the *Hubble*

Space Telescope (HST) using the Space Telescope Imaging Spectrograph (STIS), as part of the cycle 18 program #12298: 'Towards a Physical Understanding of the Diversity of Type Ia Supernovae' (PI: Ellis). The phase 2 was submitted in two parts: on 2011 August 25 for the the first few epochs, and on 2011 August 29 for the epochs from maximum light onwards. The later epochs also included parallel observations with the Wide Field Camera 3 to observe Cepheid variable stars in M101.

In this section, we describe these *HST* observations and their reduction, and detail the construction of a single spectrum on each *HST* epoch. One of these spectra has already been shown in Foley & Kirshner (2013).

2.1 *HST* spectral observations

We used five different STIS configurations using both the CCD and the UV MAMA detectors, covering 4 different wavelength ranges. On all epochs, the near-UV was covered using either NUV-MAMA/230L (giving useful coverage from $\lambda \simeq 1750$ to $\simeq 3150\text{Å}$) or CCD/230LB ($\lambda \simeq 1900$ to $\simeq 3050\text{Å}$), the optical using CCD/430L ($\lambda \simeq 2950$ to $\simeq 5700\text{Å}$), and the near-IR using CCD/750L ($\lambda \simeq 5300\text{Å}$ to $\simeq 1\mu m$). On one further epoch near maximum light an additional configuration was used to examine the far-UV (FUV-MAMA/140L $\lambda \simeq 1300$ to $\simeq 1700\text{Å}$). When using the CCD, we split the observations to assist with cosmic ray rejection ('CR-SPLIT'), and took separate flat-fields after the CCD/750L observations to assist with fringe removal. We used the $0.2''$ slit throughout. A full log of our *HST* observations can be found in Table 1.

At the time of triggering the *HST* ToO, the eventual photometric evolution of SN 2011fe, including its peak brightness and light curve width, was quite uncertain. We thus opted to use the CCD/230LB for the near maximum-light epochs in preference to NUV-MAMA/230L to avoid any possibility of exceeding the MAMA bright-object limits, even though the NUV-MAMA/230L was preferred scientifically because of its superior far-UV coverage. Exposure times, dithers and CR-SPLITs were chosen in an attempt to avoid saturation of this bright target while still efficiently filling the time available in each orbit. For the most part this was successful, although some observations were slightly saturated at the peaks of the SN spectral features because of an under-estimate of the target's eventual brightness and photometric evolution. We discuss the treatment of these saturated spectra in the next section.

2.2 Data reduction

The reduction of the *HST* data followed standard procedures. The data were downloaded from the *HST* archive using the on-the-fly reprocessing (OTFR) pipeline to provide the appropriate 'best' calibration files. As some aspects of the reduction needed to be performed 'by hand' (e.g. fringe removal in the IR data), we used a local CALSTIS installation in IRAF[1] to perform the reductions.

CALSTIS gives fully calibrated and extracted 1-D spectra, where the reduction and extraction is optimised for point sources. It performs initial 2-D image reduction such as image trimming,

bias and dark current subtraction, cosmic-ray rejection (using a CR-SPLIT), and flat-fielding. It then performs 1-D spectral extraction, followed by wavelength and flux calibrations. In addition to these standard procedures, we performed three additional steps.

The first step was the fringe frame removal for CCD/750L observations, matching fringes in the CCD/750L fringe flat-field taken with the science observations, to those in the science observations themselves. This generally proceeded satisfactorily, except for the 2011 September 13 epoch where the SN trace was offset from its standard position to allow a different set of Cepheids to be observed in the parallel observations. Unfortunately the fringe-flat position was not updated to reflect this, hence this epoch has less *HST* near-IR coverage and a ground-based Gemini IR spectrum is used in its place (Hsiao et al. 2013).

The second step was the removal of hot pixels, bad pixels, and residual cosmic rays in the data. These were identified by hand by examining the post CR-SPLIT 2-D spectral images. These image defects were then interpolated over in the dispersion direction.

The final additional step was the fixing of the saturation in some of our optical (CCD/430L and CCD/750L) data at the peaks of the SN spectral features (see Table 1). As a point source, the SN has a spatial profile of ~ 11 pixels on the CCD, which is very well aligned with the CCD rows. Where present, saturation affected only the central row of this profile. We corrected for the saturation by taking the flux ratio of the central row to four other rows in the profile (two rows above and two rows below the saturated row) at every wavelength pixel. We then fitted a polynomial function to each of these four flux ratios as a function of wavelength pixel, using only the unsaturated regions in the fit. These polynomial fits can then be interpolated across wavelength pixel regions (columns) that have saturated data, and the SN flux in the saturated central row of the profile inferred from the interpolated flux ratios. The final SN flux in the saturated row is then the weighted mean of these four values, with an error reflecting the variance in these predictions. By testing this procedure on unsaturated regions of the SN spectral profile, and comparing the interpolated flux to the actual observed one, we find an excellent level of agreement.

2.3 Combined spectra

The *HST* spectra were extracted using the standard CALSTIS 1-D spectral extraction tasks, and combined with near-IR data from Hsiao et al. (2013) where available to form a single contiguous spectrum on each epoch. Where the *HST* observations were taken at more than one dither position in a given configuration, we extract each dither position separately and then combine the 1-D spectra. This is in preference to combining the 2-D images directly, as that process is sensitive to the exact sub-pixel centering of the spatial profile on a given row. The individual exposures were rebinned to a common wavelength scale in each wavelength region: 1.6Å over 1000–2900Å (1.4Å when using the CCD/230LB), 2.8Å over 2900–5000Å, 4.9Å over 5000Å–1.1μm, and 7Å over 1.1-2.5μm. The spectra were then optimally combined, weighting by the flux errors in each input pixel.

We used overlapping regions between the spectra to ensure that the flux calibration was consistent, adopting the CCD/430L spectrum as the flux reference at each epoch. Typically, this was a 1–2 per cent correction, although for the 2011-09-13 epoch there was no useful overlap between the FUV-MAMA/140L and the CCD/230LB data, so we did not adjust the FUV-MAMA/140L flux scale. In all cases the Gemini near-IR spectra over-lapped with the *HST* CCD/750L spectra to allow a relative flux calibration between

---

[1] IRAF is distributed by the National Optical Astronomy Observatories, which are operated by the Association of Universities for Research in Astronomy, Inc., under cooperative agreement with the National Science Foundation.

Table 1. Log of the *HST* spectroscopic observations of SN 2011fe.

Epoch	MJD observation (days)	Instrument configuration	Total exposure time (s)	Comments
2011-08-28	55801.212	NUV-MAMA/230L	5400	
2011-08-28	55801.100	CCD/430L	1200	CR-SPLIT=3
2011-08-28	55801.117	CCD/750L	1002	CR-SPLIT=3
2011-08-31	55804.304	NUV-MAMA/230L	2200	
2011-08-31	55804.231	CCD/430L	1156	Dither 2x578s w/ CR-SPLIT=2. Saturation.
2011-08-31	55804.244	CCD/750L	410	CR-SPLIT=2. Slight saturation.
2011-09-03	55807.425	CCD/230LB	1320	CR-SPLIT=4.
2011-09-03	55807.438	CCD/430L	195	CR-SPLIT=3. Slight saturation.
2011-09-03	55807.444	CCD/750L	195	CR-SPLIT=3.
2011-09-07	55811.415	CCD/230LB	1060	Dither 2x530s w/ CR-SPLIT=2.
2011-09-07	55811.427	CCD/430L	160	Dither 2x80s w/ CR-SPLIT=2.
2011-09-07	55811.434	CCD/750L	80	CR-SPLIT=2.
2011-09-10	55814.417	CCD/230LB	1060	Dither 2x530s w/ CR-SPLIT=2.
2011-09-10	55814.429	CCD/430L	160	Dither 2x80s w/ CR-SPLIT=2. Slight saturation
2011-09-10	55814.465	CCD/750L	80	CR-SPLIT=2.
2011-09-13	55817.805	FUV-MAMA/140L	8540	
2011-09-13	55817.669	CCD/230LB	830	Dither 2x415s w/ CR-SPLIT=2.
2011-09-13	55817.680	CCD/430L	160	Dither 2x80s w/ CR-SPLIT=2.
2011-09-13	55817.689	CCD/750L	140	Dither 2x70s w/ CR-SPLIT=2.
2011-09-19	55823.661	NUV-MAMA/230L	2720	
2011-09-19	55823.601	CCD/430L	160	Dither 2x80s w/ CR-SPLIT=2.
2011-09-19	55823.608	CCD/750L	70	CR-SPLIT=2
2011-10-01	55835.298	NUV-MAMA/230L	2700	
2011-10-01	55835.231	CCD/430L	1200	Dither 2x600s w/ CR-SPLIT=3. Slight saturation.
2011-10-01	55835.244	CCD/750L	190	CR-SPLIT=2.
2011-10-07	55841.349	NUV-MAMA/230L	3000	Dither 2x1500s
2011-10-07	55841.281	CCD/430L	1320	Dither 2x660s w/ CR-SPIT=3. Slight saturation.
2011-10-07	55841.295	CCD/750L	310	CR-SPLIT=2. Slight saturation.
2011-10-21	55855.210	NUV-MAMA/230L	3000	
2011-10-21	55855.154	CCD/430L	1220	Dither 2x610s w/ CR-SPLIT=2.
2011-10-21	55855.168	CCD/750L	420	CR-SPLIT=2.

Table 2. Details of the mean spectra constructed on each epoch.

Epoch	Ave. MJD observation	Phase (days)[a]	Wavelength coverage
2011-08-28	55801.17	-13.1	1750Å – 2.5μm
2011-08-31	55804.25	-10.1	1750Å – 2.5μm
2011-09-03	55807.38	-6.9	1900Å – 2.5μm
2011-09-07	55811.37	-2.9	1900Å – 2.5μm
2011-09-10	55814.39	+0.1	1900Å – 2.5μm
2011-09-13	55817.67	+3.4	1265Å – 2.5μm
2011-09-19	55823.62	+9.3	1750Å – 1.02μm
2011-10-01	55835.26	+20.9	1750Å – 1.02μm
2011-10-07	55841.31	+27.0	1750Å – 1.02μm
2011-10-21	55855.18	+40.8	1750Å – 1.02μm

[a]The phase is given in days in the SN rest frame relative to maximum light in the rest-frame B-band.

the two. Here the corrections were $\sim 4 - 5$ per cent, but larger on the early epochs when the SN flux was brightening rapidly. Information on the final mean spectra can be found in Table 2.

The data were corrected for the recession velocity of M101. For M101 as a whole, this is 241 km s^{-1} (de Vaucouleurs et al. 1991), but the projected radial velocity at the SN site is $\simeq$ 180 km s^{-1} (Bosma et al. 1981; Patat et al. 2013). We used this latter value in our analysis. We correct for Milky Way (MW) extinction using the maps of Schlegel, Finkbeiner, & Davis (1998) and a Cardelli, Clayton, & Mathis (1989) extinction law. Although it is not clear that these dust maps are reliable near extended objects such as M101, the correction is small (a colour excess $E(B - V)_{mw} = 0.009$ mag) and is consistent with independent evidence from Galactic Na I and Ca II absorption features in high-resolution optical spectra of SN 2011fe (see Patat et al. 2013, who derive $E(B - V)_{mw} = 0.01$ mag). We discuss extinction caused by dust in the host galaxy in the next section.

Some narrow absorption features, presumably from material in the inter-stellar medium (ISM) along the line of sight to the SN, are present in the UV spectra of SN 2011fe, in particular Mg II at 2796Å and 2803Å, Mg I at 2853Å, Fe II at 2344Å, 2374Å, 2383Å, 2587Å and 2600Å, and various Si II and Al II features in the far-UV. These are at velocities that are consistent with the recession velocity of M101 given the STIS resolution and wavelength calibration accuracy, and are probably associated with the system causing strong Na I absorption at 180 km s^{-1} identified by Patat et al. (2013). We remove the strongest of these lines from the spectra in
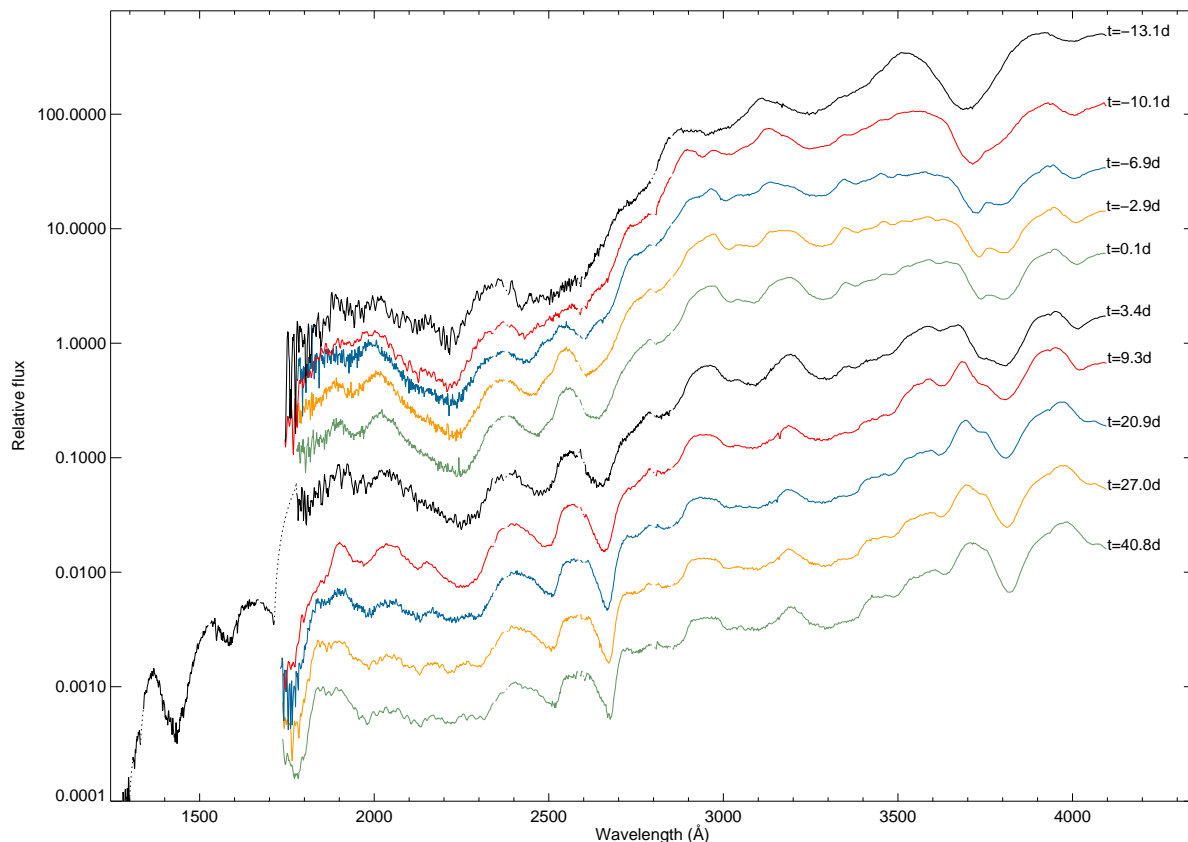
Figure 1. A time-series spectral sequence of the UV portion of the *HST* spectra of SN 2011fe. Spectra have been corrected for Milky Way extinction, corrected to the rest-frame, and had UV ISM absorption lines removed. The phase of each spectrum, marked in days relative to maximum light in the rest-frame B-band, is reported on the right. Each spectrum has been offset arbitrarily for presentation purposes.

this paper. The spectra are shown in Fig 1, and are available from the WISeREP archive[2] (Yaron & Gal-Yam 2012).

3 GENERAL PROPERTIES OF SN 2011FE

We now discuss the general optical and UV properties of SN 2011fe. In particular, we assess whether SN 2011fe is broadly representative of other SNe Ia in the UV.

3.1 Photometric properties

M101 was being observed by PTF with a daily cadence around the time of the SN 2011fe discovery. There are non-detection limits of $g > 21.2$ on MJD 55795.2 and $g > 22.2$ on 55796.2, followed by the first detection at $g = 17.3 \pm 0.01$ on MJD 55797.2. The explosion date of SN 2011fe was estimated by N11 by fitting a simple power-law model to the early-time P48 SN flux, f, as a function of time t, given by $f(t) \propto (t - t_{\rm expl})^n$, where $t_{\rm expl}$ is the explosion time and n is an exponent: $n = 2$ corresponds to a simple 'fireball' model. N11 find $t_{\rm expl} = 55796.687 \pm 0.014$ in MJD (or 2011 August 23.69), with an exponent $n = 2.01 \pm 0.01$.

A significant amount of additional optical photometry of SN 2011fe exists (Richmond & Smith 2012; Vinkó et al. 2012;

Munari et al. 2013), and is compared in detail by Pereira et al. (2013). Here, we use the SiFTO light curve fitter (Conley et al. 2008) to fit g photometry from the P48 (as this provides the earliest photometric coverage) and BVR data published by Vinkó et al. (2012). We estimate a time of maximum light in the rest-frame B-band of MJD 55814.30 ± 0.06 (2011 September 10.3), and a peak magnitude in the B-band of 9.93 ± 0.02 mag. The phases of the mean spectra on each epoch can be found in Table 2. SN 2011fe has a SiFTO light curve stretch of 0.98 ± 0.01, and from the SiFTO templates we estimate $\Delta m_{15}(B) = 1.05$ mag – although we caution this number is not a product of SiFTO and is an estimate only. Similar values have been measured by other authors (e.g. Munari et al. 2013). The $B - V$ colour, $\mathcal{C}$, at B-band maximum light is $\mathcal{C} = -0.07 \pm 0.02$. These fit parameters are all fully consistent with independent SALT-II (Guy et al. 2007) fits to SNfactory spectrophotometric data presented by Pereira et al. (2013) and, as discussed by those authors, make SN 2011fe a typical example of a normal SN Ia, and one that would be included in any standard Hubble diagram analysis had it been located in the Hubble flow (see Conley et al. 2011, for a summary of the criteria typically used).

The $B-V$ colour does not provide any evidence for extinction due to the host galaxy; if anything it is slightly blue (cf. figure 1 of Conley et al. 2011). Independent evidence for low extinction comes from Patat et al. (2013), who measure $E(B - V)_{\rm host} = 0.014 \pm 0.002$ mag. We do not correct the data for this small extinction but do account for it in our modelling.

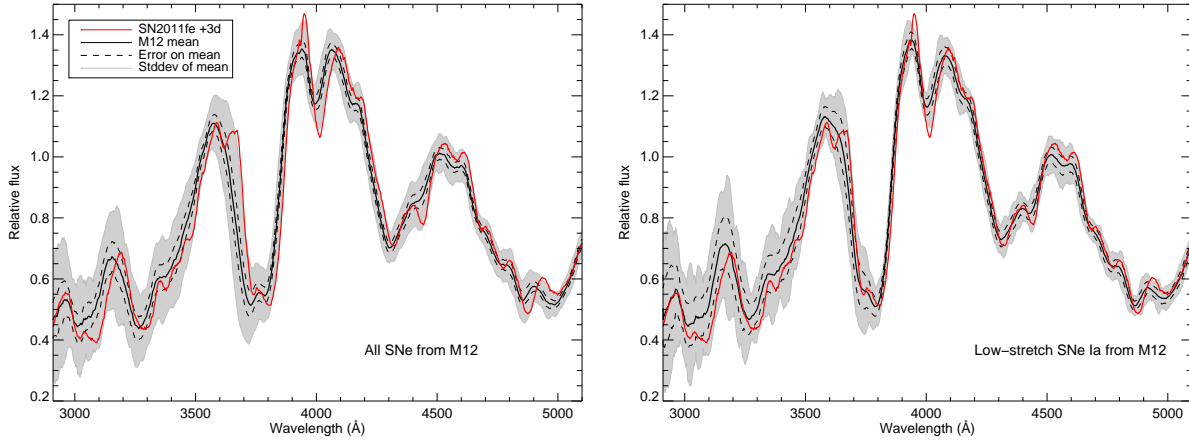The inferred rise time $t_{\rm r}$ measured from the SN light curve is

Figure 2. A comparison between the average of the +0.1 d and +3.4 d spectra of SN 2011fe, and the mean near-UV spectrum of M12 constructed from *HST* data taken at phases between -1 and +4.5 d, excluding SN 2011fe. The dashed line is the error on the M12 mean spectrum, and the shaded grey band shows the standard deviation of the input data. The spectra have been normalised using a box filter between 4000Å and 4500Å. Left: The comparison to the entire M12 sample. Right: The comparison to just the low stretch events ($s < 1.03$).

17.6 ± 0.1 d, close to the average for normal SNe Ia (Hayden et al. 2010). This is most likely a lower limit to the true t_r, i.e., the true explosion date is likely earlier than that measured from the light curve: the light-curve based t_r measurement does not take into account photon diffusion within the dense ejecta of the young SN. This can lead to a delay between the SN explosion and the emergence of the first optical photons (Piro & Nakar 2013a,b; Hachinger et al. 2013). The rise-time (or explosion date) is a critical input to our modelling as it defines the time from the explosion of the SN to each of our spectra. We assess the consistency of various values of t_r with the spectroscopic modelling in Section 5.1.

3.2 UV spectral comparisons

We compare our near-UV spectra of SN 2011fe with the mean near-UV spectrum for low redshift SNe Ia compiled from data in M12 from -1 to +4.5 d. Two of our spectra have phases in this range (Table 2) and we average them together to give a mean phase of +1.8 d. The M12 mean includes SN 2011fe in its construction, so we re-generate the mean without SN 2011fe; the average phase of the mean spectrum is +2.1 d. The comparison is shown in Fig. 2 (left-hand panel). The overall level of agreement is good, although some differences can be seen: for example, the positions/velocities of the near-UV features are systematically redder/slower in SN 2011fe compared to the mean of the M12 sample.

M12 identified a strong trend between the stretch of SNe Ia and the velocities/positions of some near-UV spectral features; higher stretch SNe Ia have bluer features. As SN 2011fe, with $s = 0.98$ (Section 3.1) would fall into the 'low stretch' sample of M12, we also compare to the mean generated from just the low-stretch SNe (Fig. 2, right-hand panel). The agreement between the UV feature positions (particularly the Ca II H&K absorption) is better, and the SN 2011fe spectrum falls within the range of spectra examined in M12.

In summary to this section, we conclude, as have others, that SN 2011fe is photometrically a fairly typical example of a SN Ia, and that this extends to its behaviour in the near-UV. Thus inferences drawn from SN 2011fe are likely to be broadly applicable to other SNe Ia.

4 MODELLING TECHNIQUE

We now turn to the modelling of the SN 2011fe spectra. We first outline our modelling framework and assumptions, and then present the models of SN 2011fe in Section 5.

4.1 Monte Carlo radiative transfer code

We model the spectra of SN 2011fe using a Monte Carlo code (Abbott & Lucy 1985; Mazzali & Lucy 1993; Lucy 1999; Mazzali 2000; Stehle et al. 2005). The code performs radiative transfer above a sharp lower boundary (or 'photosphere'). To generate a spectrum at any given epoch, the code requires as input the bolometric luminosity L_{bol}, the time t since the SN explosion (hence the importance of an accurate knowledge of t_r), the photospheric velocity v_{ph}, the density distribution of the SN ejecta in the homologous expansion phase (Section 4.4), and the abundances of the elements in the ejecta.

The code simulates the propagation of photon packets emitted at the photosphere with a black-body spectrum of temperature T_{ph} $[I_\nu^+ = B_\nu(T_{ph})]$. The SN ejecta are assumed to be optically thick below this photosphere. Although this is a relatively rough approximation, and one which at later epochs can cause an excess in the red and IR flux of the models, it makes the code flexible as quantitative abundances can be derived without a knowledge of the exact distribution of radioactive heating below the photosphere. Since all lines important for abundance determination are in the UV/optical, the poor reproduction of the near-IR continuum has only minor consequences on our results. Photon packets undergo Thomson scattering and line absorption. Following absorption, packets are immediately re-emitted in a transition chosen randomly via a branching scheme. Packets that are scattered back into the photosphere are considered to be re-absorbed. Radiative equilibrium is enforced by the 'indivisible-packet' approach (Lucy 1999). The code iterates T_{ph} (and thus the outgoing intensity at the photosphere) so as to match L_{bol} given the actual back-scattering rate.

The excitation/ionisation state of the gas is determined by the radiation field using a modified nebular approximation (Mazzali & Lucy 1993; Mazzali 2000). Starting from an initial guess, the radiation field and the state of the gas are iterated with

a series of Monte Carlo experiments until convergence is achieved. The final emergent spectrum is obtained by computing the formal integral, avoiding excessive Poisson noise (Lucy 1999).

4.2 Spectral modelling

In its simplest form, our code uses homogeneous abundances above the photosphere ('one-zone' modelling, e.g. Mazzali et al. 1993). Intermediate-mass elements (IMEs, e.g. Mg, Si, S, Ca) typically influence the strength of spectral features in the optical, whereas Fe-group elements lead to the formation of features in the optical and the UV. Additionally, Fe-group elements are essential for fluorescence and reverse-fluorescence processes, as simulated by the branching scheme (Lucy 1999). These processes can be particularly important for the formation of the UV spectrum (Mazzali 2000).

The spectral line strengths are strongly influenced by ionisation/excitation, which in turn depend on the radiation field. A lower $v_{ph}(= r_{ph}/t)$ leads to a lower r_{ph} and hence a higher temperature with a bluer radiation field at the photosphere, favouring ionisation and the occupation of highly-excited states, with lines forming at lower velocity. A higher L_{bol} has a similar effect on the temperature but not on the line velocities, apart from an indirect effect on ionisation and excitation.

The typical modelling process involves iterating L_{bol} until the flux in the observed spectrum is matched by the model; any IR excess in the model due to the photospheric black-body approximation (Section 4.1) is disregarded. Simultaneously, v_{ph} is iterated to optimise the position of the lines and the overall spectral shape. Abundances are first defined in an approximate way during this process, and may be improved once L_{bol} and v_{ph} are fixed, but since they both depend on the density structure and affect the thermal state of the gas, the two procedures are not physically independent. This also implies that it may be difficult to find a 'perfect' solution. However, the combined fit of line position and strength with the shape of the pseudo-continuum represents a quantitative solution of the physical conditions of the SN atmosphere.

4.3 Abundance tomography

Although one-zone modelling can effectively constrain abundances near the photosphere, it does not follow abundance variations with radius (or velocity). Stehle et al. (2005) introduced the technique of constraining the abundance stratification of the ejecta ('abundance tomography') by using a time-series of SN spectra. Defining the abundances as a function of ejecta depth, they used a time-series of spectra to 'observe' the different layers.

In the early, photospheric phase (up to a few weeks after maximum light in SNe Ia), the inner ejecta are optically thick. As the ejecta expand, the photosphere recedes inside the ejecta following the decreasing density, as witnessed by the decreasing blueshift of the observed spectral lines (e.g. Benetti et al. 2005). In order to obtain an optimal description of the abundance stratification in the outermost ejecta, two or three independent layers are usually introduced above the photosphere of the first spectrum. The abundances in these layers are defined by fitting the spectrum, with the edges of the layers chosen to improve the fit.

In progressively later spectra the photosphere lies at increasingly lower velocities. The abundances above the new, lower-lying photosphere (but beneath the previous one) can now be determined. This procedure is repeated with the later spectra until the abundance stratification of the layers accessible with photospheric-epoch spectra is fully described. The process requires iteration: abundances in

the outer layers determined from earlier spectra may not be optimal for the later spectra. Thus, the abundances are adapted so as to fit all spectra in the best possible way, re-calculating the entire spectral sequence to obtain a consistent model. The uncertainty in this procedure can be as much as ~ 25 per cent on the abundances, but it is usually smaller (Mazzali et al. 2008).

The inner layers can only be analysed using nebular spectra, which are needed to obtain a complete picture and conclude the abundance tomography procedure (Stehle et al. 2005). The nebular spectra of SN 2011fe will be analysed in a future article.

4.4 Density profiles

One of the most critical ingredients in this process is the assumed density profile of the SN ejecta, which itself is the product of a particular explosion model. For example, a density profile with higher densities in the outer layers of the ejecta can lead to enhanced absorption in the spectral regions sensitive to these layers. The UV is a particularly sensitive region because the large number of overlapping metal lines causes the opacity to be higher than in the optical. Accordingly, we tested various profiles from different explosion models on SN 2011fe. We started with models W7 and WS15DD1 (Nomoto et al. 1984; Iwamoto et al. 1999), as they appear to be the most appropriate for SN 2011fe, which does not show strong absorption at high velocities. These density profiles formally correspond to a single-degenerate explosion scenario; we are not able to test double degenerate scenarios as their density profiles are not available. However, judging from the plots in (Röpke et al. 2012) the outer layers appear quite different from those of a delayed detonation in both density and composition. Other differences may be revealed at late times (e.g. Mazzali et al. 2011).

W7 is a parametrised 'fast deflagration' model, with kinetic energy $E_K = 1.3 \times 10^{51}$ erg. Although it may be considered unphysical because of its parametrisations, W7 represents a useful benchmark, and its density distribution has been successfully used to reproduce light curves and spectra of normal SNe Ia (e.g. Stehle et al. 2005; Mazzali et al. 2008). Delayed-detonation models, where an initial deflagration turns into a supersonic detonation at some point during the explosion (Khokhlov 1991), may be considered more realistic. Although the physics of the transition are still unclear, these models produce explosion energies and abundance stratifications that match SN Ia observations (Mazzali et al. 2007; Tanaka et al. 2011; Röpke et al. 2012). In particular, they pre-expand the white dwarf in the deflagration phase, so that the subsequent detonation produces not only Fe-group elements, but also IMEs, which are ejected at realistic velocities. WS15DD1 (hereafter WDD1) is a low-energy delayed-detonation model (Iwamoto et al. 1999) with $E_K = 1.33 \times 10^{51}$ erg and synthesised ^{56}Ni mass $M(^{56}\text{Ni}) = 0.56\,M_\odot$, which is a good match to values derived from the bolometric light-curve of SN 2011fe (Pereira et al. 2013).

The density profiles of all models used in this paper are shown in Figure 3. Our models are most sensitive to the density profile in the outer ejecta, and thus the difference between the amount of material at high velocity in W7 and WDD1 is important for our models. WDD1 has more material at high velocity, reflecting the passage of the detonation shock. Based on the effect density profiles have on the UV, we also built a third, 'intermediate' density profile which yields better fits to the spectra than either W7 or WDD1. We call this model 'ρ-11fe' (Section 5.3).
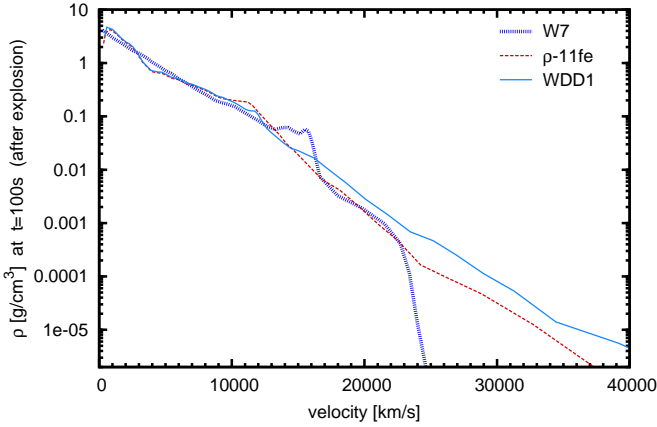
Figure 3. The SN ejecta density profiles of the W7 and WS15DD1 (WDD1) models discussed in Section 4.4 (Iwamoto et al. 1999), and of the ρ-11fe model constructed to optimise the comparison between the synthetic spectra and observed data (Section 5.3).

5   SPECTRAL MODELLING OF SN 2011FE

Our goal is to model the spectral data for SN 2011fe using the framework outlined in Section 4. Our base models assume a metallicity of 0.5 $Z_\odot$, motivated by the metallicity of M101 at the position of SN 2011fe (Stoll et al. 2011). We explore this assumption in Section 6.1.

The first step is to determine the rise time (t_r) from the models independently from the t_r measured from the photometry (Section 3.1). This requires very early spectral data, where the leverage on the explosion epoch is largest and the statistical uncertainty consequently smallest (Mazzali 2000) – a small absolute change in t_r is large in relative terms. We make use of an early low-resolution spectrum taken with the Telescopio Nazionale Galileo (TNG) on 2011 August 25 (MJD 55799.0) and previously presented in N11 and analysed in Parrent et al. (2012). The spectrum of SN 2011fe shown here differs from the previously published version as it has been recalibrated with a more optimum extraction of the spectophotometric standard star. This process has made the flux calibration in the blue more reliable and we now feel more confident about the calibration down to 3500 Å. The redder wavelengths of the spectrum are unaffected. The value of t_r that provides the best fit is then used to model the spectra at later epochs.

We did not use two earlier spectra of SN 2011fe that are also available (see Parrent et al. 2012). The LT and Lick spectra of 2011 August 24 are affected by high velocity features (HVFs). These are weak compared to other SNe Ia (Mazzali et al. 2005, e.g.) and are not detached from the photospheric component, but do cause a significant blueshift of the observed features (Parrent et al. 2012). This makes it difficult to locate precisely the position of the photosphere, and hence to produce accurate models, without a detailed knowledge of the ejecta properties that lead to the generation of these HVFs. We defer this more complex analysis to a later paper.

5.1   Testing the rise time

Early-time spectra of SNe can be used to estimate the time of the explosion (Mazzali & Schmidt 2005). The combination of L_{bol}, temperature (which depends on L_{bol} and radius r), and velocity of the absorption lines (which depends on r and t) can give powerful constraints on t_r. For both the W7 and WDD1 profiles, we computed spectral models on epochs ranging from 2.3 to 5.3 d, cor-

responding to rise times from 17.6 d (N11), which we regard as a lower limit, to 20.6 d, in steps of 0.5 d. A selection of these different t_r models is shown in Fig. 4. The different assumed epochs require different values of v_{ph}. The line velocities reflect the time evolution of the density profile, and thus in particular the assumed t_r (Hachinger et al. 2012). For a larger t_r, the spectra will be older, and thus the ejecta density in the model will be lower; v_{ph} is therefore lower and the lines less blueshifted. Note that v_{ph} is not exactly inversely proportional to t, as would be predicted by a simple Stefan-Boltzmann law. In models with higher t or lower v_{ph} (i.e. a photosphere deeper in the density profile, which rises steeply inwards) the back-scattering rate of photons would be strongly increased if one assumed $v_{ph} \sim t^{-1}$. Therefore, a realistic photosphere for such a model, avoiding an excessive temperature increase at the photosphere (via strong back-warming to maintain the outwards photon flux), must lie at a higher velocity.

For the August 25 spectrum, v_{ph} lies between $\sim$ 10000 and 18000 km s^{-1}, depending on density profile and t_r. We chose values that yield the same radiation temperature at the photosphere (T_{ph}) in all models with the same density profile: $\sim$10800 K for models based on W7 and $\sim$10300 K for models based on WDD1. This ensures that the ionisation/excitation state is similar in all models. Two abundance zones were used above v_{ph}, with the boundaries between these zones at 19400 km s^{-1} for W7 and at 18100 km s^{-1} for WDD1. Abundances were optimised for the models with t_r=19.1 d and not further modified; this has only a minor influence on the results.

The optimum t_r is taken as the one where the line positions in the model spectra best match the line positions in the observations. This is only possible if the lines measured do not exhibit strong HVFs (Mazzali et al. 2005). In the TNG spectrum the HVFs are present only in the Ca lines, and we exclude these from the determination of t_r.

We measured the positions[3] of features that are strong in the first spectrum and well reproduced in the models (marked in Fig. 4), as in Hachinger et al. (2012). Table 3 gives the wavelength offset $\Delta\lambda = \lambda_{model} - \lambda_{obs}$ for the two different models and the spectral features. Fitting a regression line to the $\overline{\Delta\lambda_{rel}}$–$t_r$ relation (where $\overline{\Delta\lambda_{rel}}$ is the mean of the relative wavelength offsets $\Delta\lambda_{rel} = \frac{\Delta\lambda}{\lambda_{obs}}$ of the features at fixed t_r), we determine the value of t_r for which $\overline{\Delta\lambda_{rel}} = 0$. We obtain an optimum t_r of 19.1 d for W7 and 19.5 d for WDD1, with a statistical error of $\simeq$ 0.5 d in both cases. The relation $\overline{\Delta\lambda_{rel}}$–$t_r$ in Table 3 is obviously influenced by errors in the measured feature centroids on a scale $\Delta t_r \lesssim 0.5$ d (see e.g. the similar $\overline{\Delta\lambda_{rel}}$ values for the W7 models with 20.1 d and 20.6 d), but on larger time scales it is well-behaved.

The quality of the spectral models depends on the shape of the entire spectrum, and not just on the match in the measured wavelength. Spectra computed for a long t_r (20.6 d) do not match the data. They are too red, reflecting the fact that the photosphere is too deep, causing too much absorption. The WDD1 model for a short t_r (17.6 d) shows features that are too blue and weak, as the mass above the photosphere is too small. The spectrum computed with

---

[3] Line-positions are measured as a line centroid wavelength, calculated as $\lambda_c = \frac{\int_{\Delta\lambda} FD^3(\lambda)\lambda d\lambda}{\int_{\Delta\lambda} FD^3(\lambda)d\lambda}$, where $FD^3(\lambda)$ is the third power of the fractional depth at λ (cf. Hachinger et al. 2008). Integrals run over the range $\Delta\lambda$ in which the line absorbs. We use the centroid instead of the deepest point (as in Hachinger et al. 2008) as the centroid can be more reliably determined when feature shapes are irregular and show considerable fluctuations within the model series, as is the case for our very early-epoch models here.
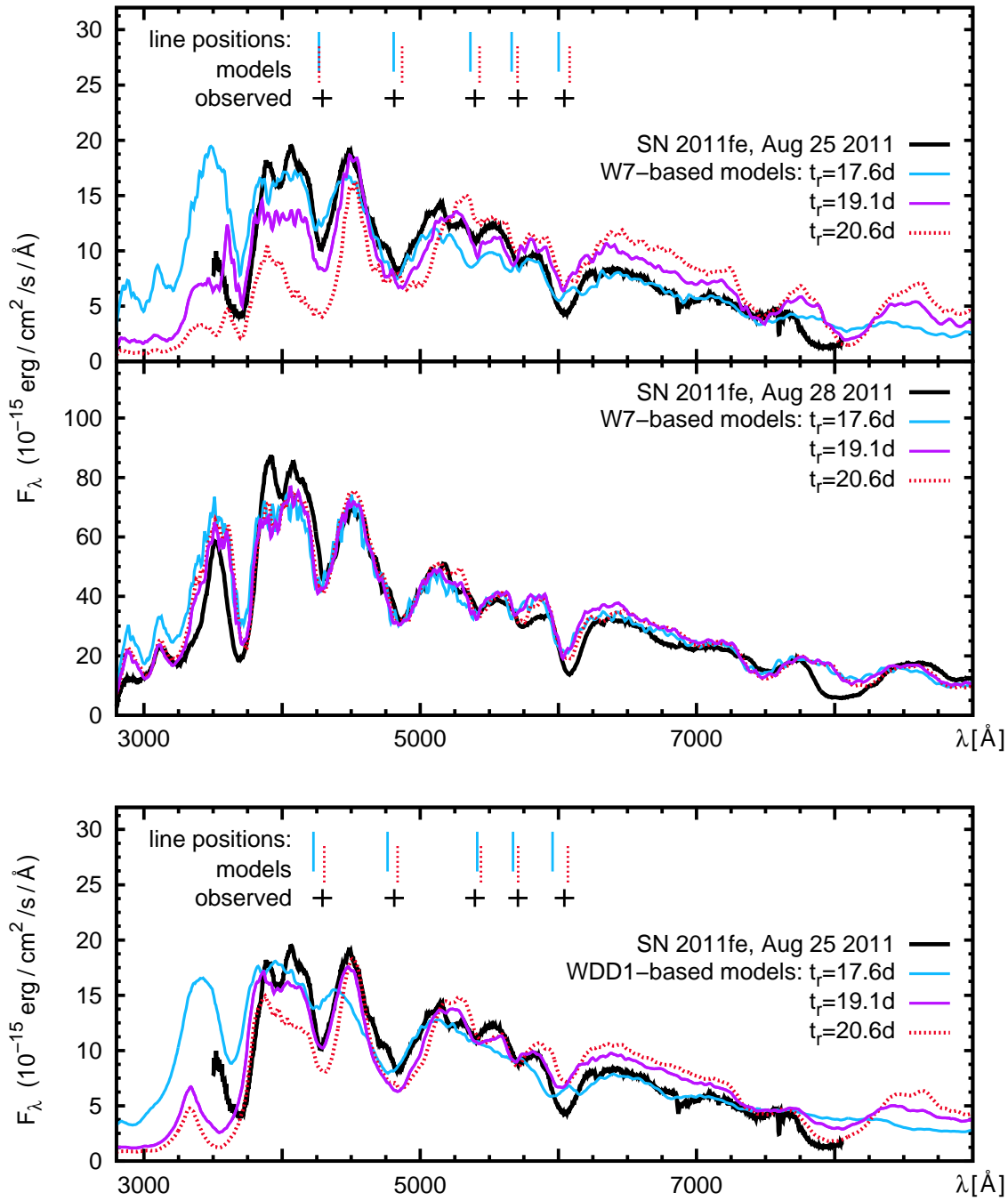
Figure 4. Early-time models for SN 2011fe computed for rise times t_r ranging from 17.6 to 20.6 d. Models in the *upper panel* were computed with the W7 density profile, models in the *lower panel* are based on WDD1. The best-fitting t_r is determined from the 2011 August 25 spectrum, where t_r has the largest effect: the middle panel shows the W7 models for the 2011 August 28 spectrum, which are less sensitive to t_r. The positions of prominent features in the spectra are marked as black crosses, and the corresponding model features also marked. For $t_r=17.6$ d, the model spectral features are on average too blue; this is no longer the case when a longer t_r is used.

the W7 model for $t_r = 17.6$ d shows somewhat high velocities in the features, but otherwise it is compatible with the data, leading to a smaller t_r estimate for W7 than for WDD1.

Although the optimum t_r somewhat depends on the density profile used, and so some small systematic uncertainty (some 0.1 day) may be expected, it is always larger than 17.6 d by $\gtrsim 1$ d. This suggests that SN 2011fe exploded earlier than inferred by fitting a power-law model to the early light curve. This delay is a simple

effect of photon diffusion: visible light is produced by the thermalisation of the γ-rays and the deposition of the energy of the positrons emitted in the decay of ^{56}Ni. At early phases, when the density is high, these processes take place essentially locally in the region where ^{56}Ni dominates, typically in the deeper layers of the ejecta. Optical photons must then diffuse out of the ejecta before they can be observed. This requires time, given the high density and consequently high opacity in the inner ejecta.

Table 3. Rise time (t_r) determination from fits to the 2011 August 25 SN 2011fe spectrum, with the offset between synthetic and observed spectral features, $\Delta\lambda = \lambda_{\rm model} - \lambda_{\rm obs}$ and the average relative offset, $\overline{\Delta\lambda}_{\rm rel}$ (cf. text). The fact that features do not always follow the overall trend of being less blueshifted for larger t_r reflects the uncertainties in determining model line velocities.

t_r	$\Delta\lambda$(Fe / Mg ~ 4300 Å) (Å)	$\Delta\lambda$(Fe / etc. ~ 4800 Å) (Å)	$\Delta\lambda$(S II $\lambda5640$) (Å)	$\Delta\lambda$(S II $\lambda5972$) (Å)	$\Delta\lambda$(Si II $\lambda6355$) (Å)	$\overline{\Delta\lambda}_{\rm rel}$ (%)
			W7-based models			
17.6	−25.1	−5.1	−33.8	−46.0	−42.1	−0.56
18.1	−16.5	2.6	−19.9	−45.9	−28.4	−0.39
18.6	−3.6	10.8	−0.2	−37.8	−18.5	−0.17
19.1	10.0	15.7	11.8	−35.4	−0.3	0.03
19.6	15.1	30.6	26.3	−17.6	18.0	0.29
20.1	3.6	47.8	41.8	−21.1	22.3	0.37
20.6	−23.9	57.2	33.6	−2.9	37.5	0.37
		regression line fit to $\overline{\Delta\lambda}_{\rm rel}$–$t_r$ relation $\Rightarrow$ $\overline{\Delta\lambda}_{\rm rel} \simeq 0$ for $t_{\rm r,W7} \simeq 19.1$ d				
			WDD1-based models			
17.6	−53.9	−46.8	0.5	−52.4	−87.1	−0.92
18.1	−33.2	−27.2	−16.0	−48.4	−68.1	−0.72
18.6	−17.9	−18.0	−7.3	−37.1	−44.6	−0.46
19.1	−2.8	−4.4	24.3	−26.8	−17.8	−0.09
19.6	8.5	8.7	45.0	−21.2	−4.6	0.15
20.1	8.8	15.0	42.5	−11.2	13.3	0.27
20.6	14.4	25.9	53.5	−1.6	20.3	0.43
		regression line fit to $\overline{\Delta\lambda}_{\rm rel}$–$t_r$ relation $\Rightarrow$ $\overline{\Delta\lambda}_{\rm rel} \simeq 0$ for $t_{\rm r,WDD1} \simeq 19.5$ d				

We conclude that while a fit to early light curve data can only set a lower limit on t_r, with spectral modelling it is possible to improve this estimate. The accuracy of the result depends on the availability of early spectral data. However, in the presence of any HVFs that affect the spectra, standard explosion models that are unable to reproduce these HVFs make it difficult (if not impossible) to determine t_r without a detailed modelling of the outermost layers of the SN ejecta (Tanaka et al. 2008).

5.2   W7- and WDD1-based spectral models

Having used an early spectrum to determine t_r, we now analyse the *HST* time series using the W7 and WDD1 densities (Figs 5 and 6, respectively). Model parameters are compiled in Table 4. We do not use the last three *HST* spectra (Table 2), as our code is optimised for the early photospheric phase, around and prior to maximum light, and these spectra are later than 20 days after peak.

For the spectrum of 2011 August 25 we used $v_{\rm ph}$ as used in the models for the determination of t_r. For W7 we used an epoch $t = 3.8$ d and $v_{\rm ph} = 14150\,{\rm km\,s^{-1}}$, for WDD1 $t = 4.2$ d and $v_{\rm ph} = 12650\,{\rm km\,s^{-1}}$. Despite the very early epoch and the high $v_{\rm ph}$, strong Si II lines are visible, indicating the presence of burned material in the outer layers. In order to reproduce these lines, the W7 models require > 30 per cent of the ejecta mass above $v_{\rm ph}$ to be material heavier than oxygen. This is only ~ 13 per cent in the WDD1-based model. Most of the burned material consists of IMEs ($9 \leqslant Z \leqslant 20$), but traces of Fe-group elements are also present. Line blanketing in the UV, which is mostly due to overlapping lines of Fe-group elements, is much stronger in WDD1 than in W7, as the delayed-detonation places more material at high velocity. WDD1 yields a better reproduction of the peak around 4000 Å, although neither model matches the feature well. This may be a consequence of our assumption of black-body emission at the photosphere. How-

ever, more sophisticated models that do not make that assumption also have difficulties reproducing this high peak, which is seen in several SNe Ia. Overall, both models reproduce the observed features reasonably well except for Si II $\lambda6355$, which is always too weak. Increasing the Si abundance above the photosphere to correct this results in too much high-velocity Si absorption at later epochs. Hints of a HVF are visible in the Ca II IR triplet, as confirmed at later epochs. As discussed above, we do not try to match these HVFs, although they may be the reason for the strength of the Si II line in this spectrum.

Note that $v_{\rm ph}$ is larger in the W7 model than in the WDD1 one. This may seem counter-intuitive, as W7 has less mass at high velocity. The reason for selecting a higher $v_{\rm ph}$ for W7 is that because of the smaller mass at high velocity, the UV opacity is smaller and hence the UV flux higher than in WDD1 if similar $v_{\rm ph}$ are used. By selecting a higher $v_{\rm ph}$ the temperature is reduced and the UV flux decreases. This is obviously not an ideal solution, since the line velocities are then too high, but it shows that W7 does not have the correct density distribution at high velocities.

On 2011 August 28 the first UV spectrum was observed by *HST*. Having the UV available constrains our models significantly. Although both density profiles provide a good fit in the optical, the synthetic spectra show large differences in the UV. In particular, the low flux level at $\lambda \lesssim 2500$ Å can only be reproduced if there is sufficient material at high velocity to absorb photons, which is a feature of delayed-detonation models (Iwamoto et al. 1999). Features in the UV are dominated by singly-ionised Fe-group elements and Mg (Fig. 5). Ni, Fe, Ti / V / Cr[4] and Mg influence different parts

---

[4] The lines of Ti, V, and Cr are too heavily blended for us to be able to distinguish the influence of each element. Therefore we determined a combined abundance, with a mix similar to the results of nucleosynthesis models (Iwamoto et al. 1999).

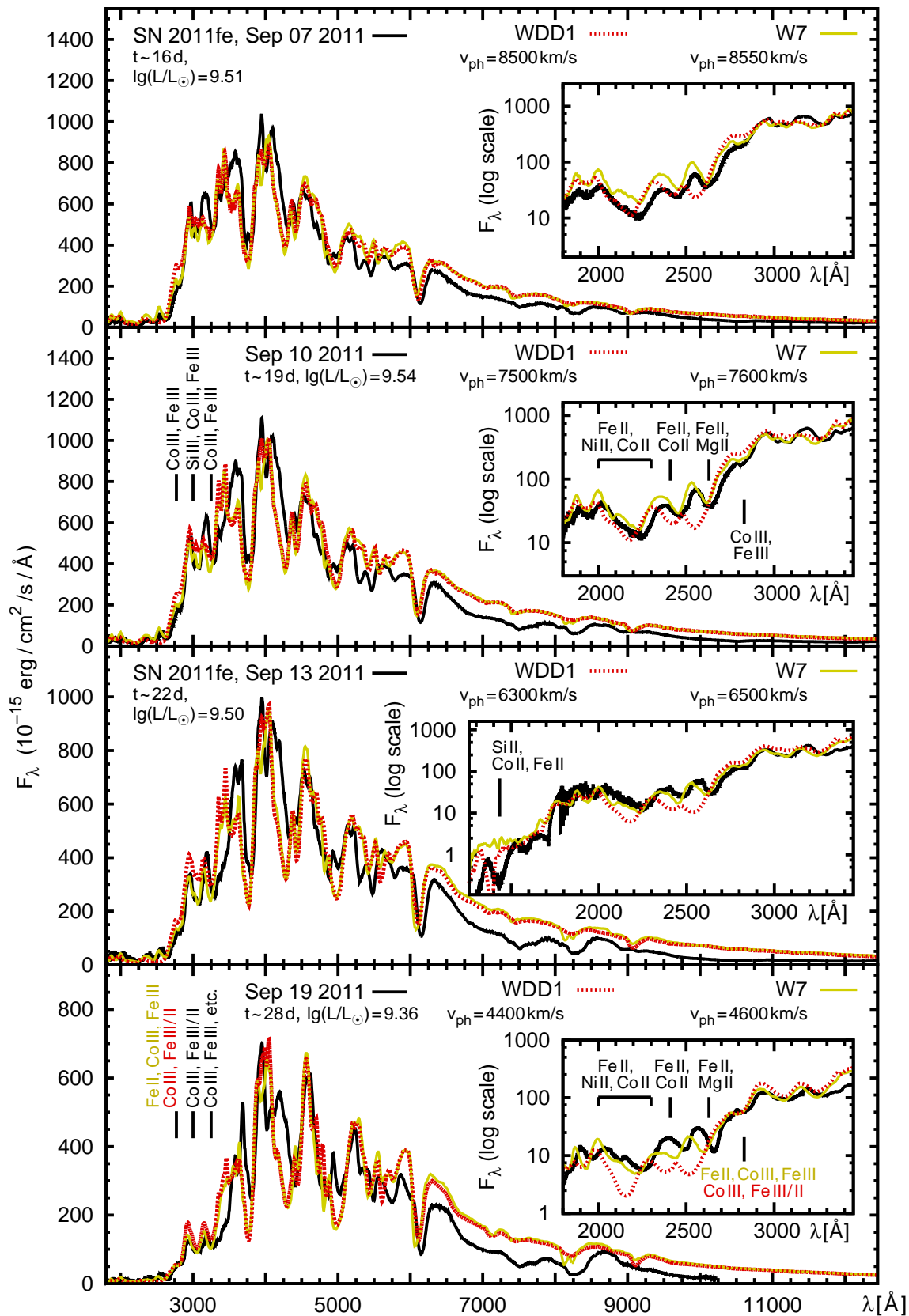**Figure 5.** Spectra of SN 2011fe (black lines) compared to models based on the W7 and WDD1 density profiles (yellow / light grey, solid lines; red / grey, dotted lines, respectively). Insets show the UV in more detail (with logarithmic flux axis). The models have been reddened by $E(B - V)_{\rm host} = 0.014$ mag. The ions responsible for the most prominent UV features in our model are marked, in order of importance.

Figure 6. The W7 and WDD1 model sequences, continued.

Table 4. Luminosities, photospheric velocities and temperatures of the photospheric black-body in the W7 and WDD1 models.

Date (UTC)	Phase (days)	t (days)	$L_{\rm bol}$ ($10^9 {\rm L}_\odot$)	$v_{\rm ph}$ (km s^{-1})	$T_{\rm ph}$ (K)
			W7		
Aug. 25	-15.3	3.8	0.08	14150	10800
Aug. 28	-13.1	6.0	0.32	12900	12100
Aug. 31	-10.1	9.1	1.1	11150	14600
Sept. 3	-6.9	12.2	2.3	10200	15200
Sept. 7	-2.9	16.2	3.2	8550	15100
Sept. 10	$+0.1$	19.2	3.5	7600	14500
Sept. 13	$+3.4$	22.5	3.2	6500	14000
Sept. 19	$+9.3$	28.4	2.3	4600	13500
			WDD1		
Aug. 25	-15.3	4.2	0.08	12650	10300
Aug. 28	-13.1	6.4	0.32	11650	12400
Aug. 31	-10.1	9.5	1.1	10650	14500
Sept. 3	-6.9	12.6	2.3	10100	14800
Sept. 7	-2.9	16.6	3.2	8500	15100
Sept. 10	$+0.1$	19.6	3.5	7500	14800
Sept. 13	$+3.4$	22.9	3.2	6300	14400
Sept. 19	$+9.3$	28.8	2.3	4400	13600

of the spectrum, so that their abundances can be determined independently. The different UV features are discussed in more detail in Section 5.3.

The next two spectra were obtained on 2011 August 31 and 2011 September 3 ($\sim$ 9–13 d after explosion) when the SN was significantly more luminous. Between 2700 and 3500 Å, absorption by doubly-ionised Fe-group species now appears. The photosphere is now in the incompletely burned region ($10100 - 11150$ km s^{-1}), where the two models differ less in density. At both epochs, the synthetic spectra match the observed ones reasonably well. Most differences are in the UV. The positions of the UV features of the W7 model agree with the observed ones, but the overall flux is generally too high, implying too little absorbing material, as discussed above. The WDD1-based model reproduces the overall flux, but the Fe-group lines are too blueshifted because of the increased high-velocity absorption introduced by even a weak delayed-detonation model. In both models, the regions just above the photosphere contains up to 6 per cent Fe by mass (this is so high that it is likely to be Fe synthesised in the explosion), while the mass fraction of ^{56}Ni, including the decay products ^{56}Co and ^{56}Fe (which is however negligible at this early phase), is between 11 and 30 per cent. The dominant constituents in this region are, however, IMEs. The carbon abundance at these velocities has dropped to zero. A weak C II line may still be present at $\sim$ 6580 Å in the observations: this can be reproduced by the carbon in the outer layers.

By maximum light (the 2011 September 7 and 2011 September 10 spectra; Fig. 6), the photosphere has receded about half way inside the ejecta ($v_{\rm ph} \sim 7500 - 8600$ km s^{-1}). The value of $L_{\rm bol}$ at maximum is in good agreement with that derived by Pereira et al. (2013). In these layers ^{56}Ni dominates, and little incompletely burned or unburned material remains. In the UV, where the fit is very good, Co lines play a larger role as ^{56}Ni decays. The slight mismatch between models and observations in the red and IR, where the models show a small flux excess, is probably a consequence of the black-body approximation at the photosphere in a low electron density environment (Section 4.1).

At post-maximum epochs, (2011 September 13 and 19, $\sim$ 23

and 29 d after explosion, respectively, Fig. 6), the largest differences between W7 and WDD1 are again in the UV. The W7 model now gives a somewhat better match. In the near-UV, the absorptions of the WDD1 model are too blue and the UV flux too low, again indicating too much opacity at high velocities. The WDD1 model is in better agreement with the data in the far-UV ($\lambda < 2000$ Å) in the 2011 September 13 spectrum, the only epoch for which far-UV data are available. However, it may be affected by too much backwarming, again a consequence of the large mass at high velocities: this can be seen in the excessive Si III 5740 Å absorption.

The September 19 spectrum can be modelled using $v_{\rm ph} = 4600$ km s^{-1} for W7 or 4400 km s^{-1} for WDD1. The material at this depth is very rich in ^{56}Ni, and a more reliable analysis of these zones should be made using nebular spectra.

5.3 The 'ρ-11fe' model

Spectra produced with the W7 density profile have too much flux in the UV. On the other hand, spectra produced with WDD1 have the correct UV flux level but the UV features are typically too blue when compared to the observations. It is interesting however to notice that the two models are practically indistinguishable in the optical (see also Röpke et al. 2012), highlighting the importance of the UV as a diagnostic. Previous modelling of combined UV/optical spectra of SNe Ia (e.g. Sauer et al. 2008b; Walker et al. 2012) suggests that the discrepancies are due to the lack of material at high velocity in the case of W7, and to an excess of such material in the case of WDD1. In fact, the layer with $v > 24000$ km s^{-1} is the region where the two models disagree most strongly (see Fig. 3). We therefore constructed arbitrary density structures that try to address these issues, and tested their spectral behaviour. We show here the results of the best of such models, which we call "ρ-11fe". This is essentially a rescaled version of WDD1 with a steeper high-velocity tail and therefore less mass at the highest velocities. Thus, ρ-11fe may be thought of as a very weak delayed detonation, although other models may show similar properties. The model is shown in Fig.3 along with W7 and WDD1. Formally, ρ-11fe has $E_K = 1.23 \times 10^{51}$ erg, which is less than both W7 and WDD1, but here we can only test the outer part of the ejecta, so this result must be taken with caution. The high-velocity layers of ρ-11fe carry little mass (0.003 M$_\odot$ above 24000 km s^{-1}) and energy (0.02×10^{51} erg in the same zone).

As a first check of ρ-11fe, we performed the same rise-time test as for W7 and WDD1 (Section 5.1), setting $T_{\rm ph} = 10800$ K, which seems to give an optimal match to the 25 Aug spectrum. Synthetic spectra for the different rise times are shown in Fig. 7 and line offsets are given in Table 5. We allowed generously large timesteps between the various models. While the longer risetime clearly results in a very red spectral distribution, incompatible with the observations, the two shorter risetimes yield reasonable results. UV data would increase the leverage of this technique. If we test the position of the absorption features we infer an optimum rise time of $t_{\rm r} = 19.0 \pm 0.5$ d, similar to the values obtained for W7 and WDD1. We modelled the spectral time series using this value.

The synthetic spectra for the model series are shown in Figs 8 and 9. Model parameters and physical properties are listed in Table 6. As expected, the ρ-11fe model spectra are intermediate between the W7 and WDD1 spectra. They show an overall better reproduction of the spectral distribution. The largest differences with respect to the W7 and WDD1 models are in the UV, but it is interesting that several features in the optical are also improved.

At the earliest epochs (2011 August 25, 28 and 31), ρ-11fe
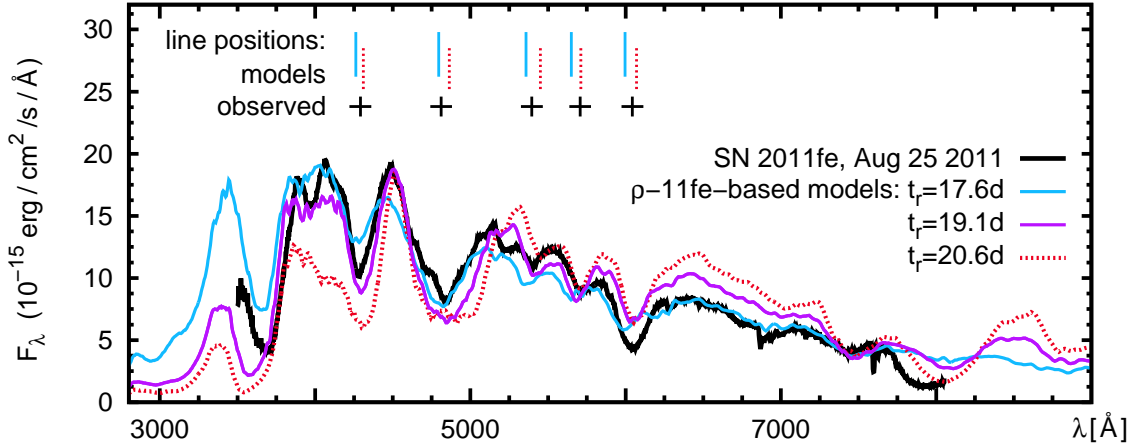
Figure 7. Early-time models for SN 2011fe based on the ρ-11fe density profile, assuming different rise times t_r between 17.6 d and 20.6 d. The optimum rise time is determined comparing the positions of prominent features in the optical between observed spectrum (black crosses) and models (light blue/grey, solid lines for 17.6 d; purple/dark grey, solid lines for 19.1 d; red/dark grey, dotted lines for 20.6 d) – analogous to Fig. 4.

Table 5. As Table 3, but for the ρ-11fe model.

t_r	$\Delta\lambda(\text{Fe}/\text{Mg} \sim 4300\,\text{Å})$ (Å)	$\Delta\lambda(\text{Fe}/\text{etc.} \sim 4800\,\text{Å})$ (Å)	$\Delta\lambda(\text{S II } \lambda5640)$ (Å)	$\Delta\lambda(\text{S II } \lambda5972)$ (Å)	$\Delta\lambda(\text{Si II } \lambda6355)$ (Å)	$\overline{\Delta\lambda}_{\text{rel}}$ (%)
			ρ-11fe-based models			
17.6	-29.0	-15.8	-37.9	-57.2	-47.8	-0.70
18.1	-15.2	-4.7	-21.4	-34.5	-28.9	-0.39
18.6	0.1	3.7	1.5	-27.5	-14.5	-0.12
19.1	12.0	15.9	13.6	-20.0	10.9	0.14
19.6	21.2	21.2	30.7	-11.9	7.8	0.28
20.1	23.8	41.2	44.4	-4.4	18.5	0.49
20.6	18.7	52.5	55.6	3.7	26.5	0.61
		regression line fit to $\overline{\Delta\lambda}_{\text{rel}}$–$t_r$ relation $\Rightarrow$ $\overline{\Delta\lambda}_{\text{rel}} \simeq 0$ for $t_{r,\rho\text{-11fe}} \simeq 19.0$ d				

shows stronger UV absorption than W7, but the features are formed at somewhat longer wavelength than with WDD1, improving the quality of the fit. Further optimisation of the density profile may lead to an even better match. This would require an accurate study of the density in the outermost layers, including the modelling of HVFs, which we defer to later work. Additionally, 3D effects may not be negligible in the outermost layers (Tanaka et al. 2006).

Since the ad-hoc density profile we constructed yields improved fits to the UV-optical spectra up to several days after maximum, we can use it to diagnose abundances in the outer layers of SN 2011fe. The Ni/Co/Fe blend near 2000–2300 Å is a diagnostic for radioactive material from the $^{56}\text{Ni} \rightarrow ^{56}\text{Co} \rightarrow ^{56}\text{Fe}$ decay chain, and its shape shows some sensitivity to ^{56}Ni even in the outer ejecta. The Fe abundance can be constrained from Fe-dominated features such as the near-UV blend near 3300 Å and from the optical Fe features. If the Fe abundance turns out to be larger than the estimated abundance in the progenitor, the abundance of stable Fe synthesised directly in the explosion can also be tested, since at early times little ^{56}Ni has decayed to ^{56}Fe. The UV spectra thus allow us to constrain the abundances of both Fe and ^{56}Ni in the outer part of the SN ejecta (cf. Hachinger et al. 2013).

Table 6. Luminosities, photospheric velocities and temperatures of the photospheric black-body in the ρ-11fe model (analogous to Table 4).

Date (UTC)	Phase (days)	t (days)	L_{bol} $(10^9 \text{L}_\odot)$	v_{ph} (km s^{-1})	T_{ph} (K)
			ρ-11fe		
Aug. 25	-15.3	3.7	0.08	13300	10800
Aug. 28	-13.1	5.9	0.32	12400	12100
Aug. 31	-10.1	9.0	1.1	11300	14500
Sept. 3	-6.9	12.1	2.3	10700	14900
Sept. 7	-2.9	16.1	3.2	9000	15100
Sept. 10	$+0.1$	19.1	3.5	7850	14700
Sept. 13	$+3.4$	22.4	3.2	6700	14100
Sept. 19	$+9.3$	28.3	2.3	4550	13500

5.4 Abundances

The one-dimensional abundance stratification we infer for SN 2011fe using the ρ-11fe profile is shown in Fig. 10 (bottom panel). Although it bears similarities to the nucleosynthesis of W7, a 1D deflagration model (Iwamoto et al. 1999; Fig. 10, top panel), there are significant differences in the degree of mixing, in particular at intermediate velocities, the composition of which is very reminiscent of WDD1, a 1D delayed-detonation
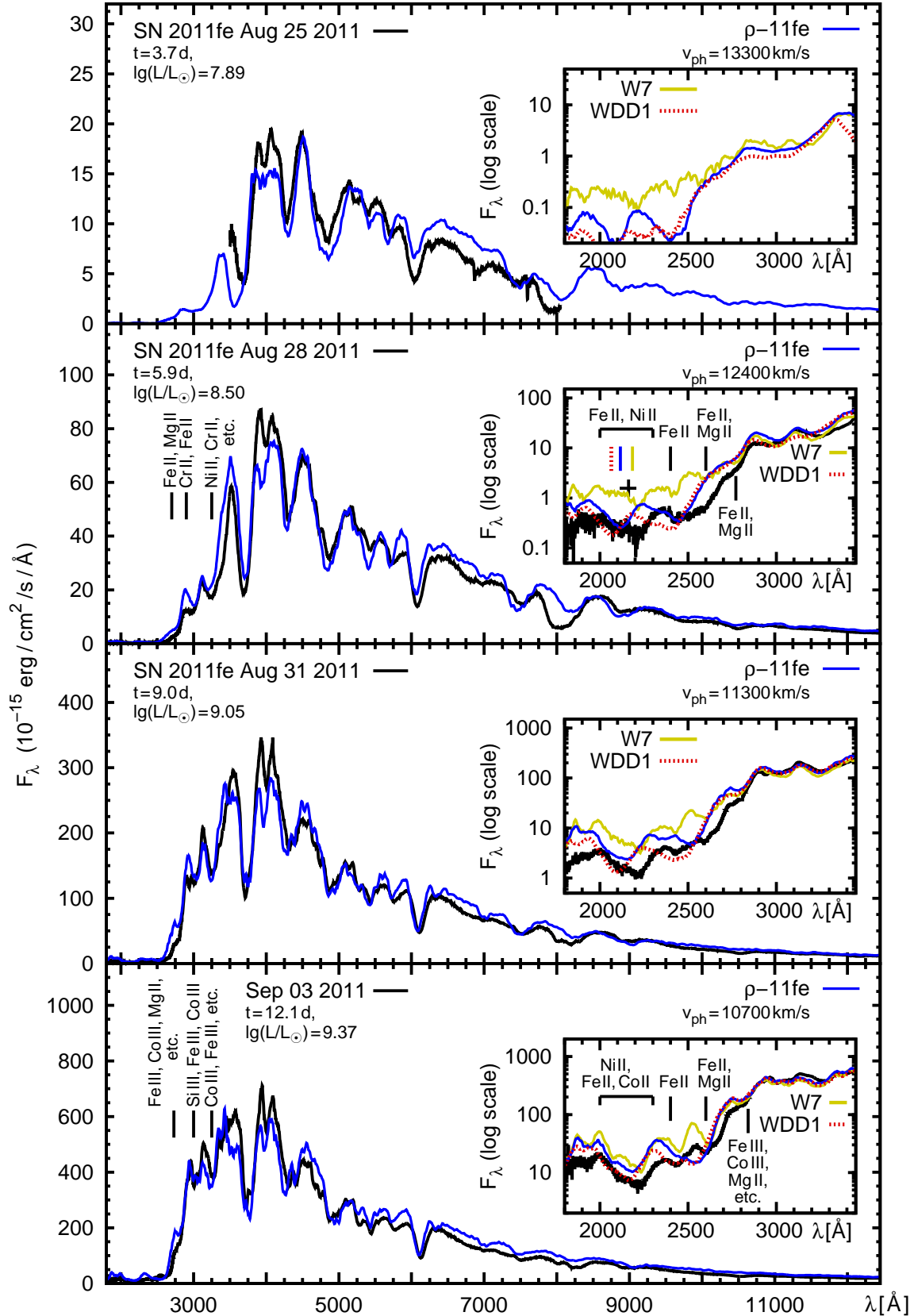
Figure 8. Spectra of SN 2011fe (black lines) compared to models based on the ρ-11fe density profile (blue, solid lines). The insets also show the W7-based models (yellow, solid lines) and the WDD1-based models (red, dotted lines) for comparison. The inset for Aug 28 demonstrates that ρ-11fe reproduces the observed line positions (observed centroid of 2000–2300 Å feature marked with a cross; model feature centroids marked with tics) somewhat better than WDD1. W7 reproduces the line positions practically perfectly, but has too low a UV opacity to reproduce the observed UV flux.
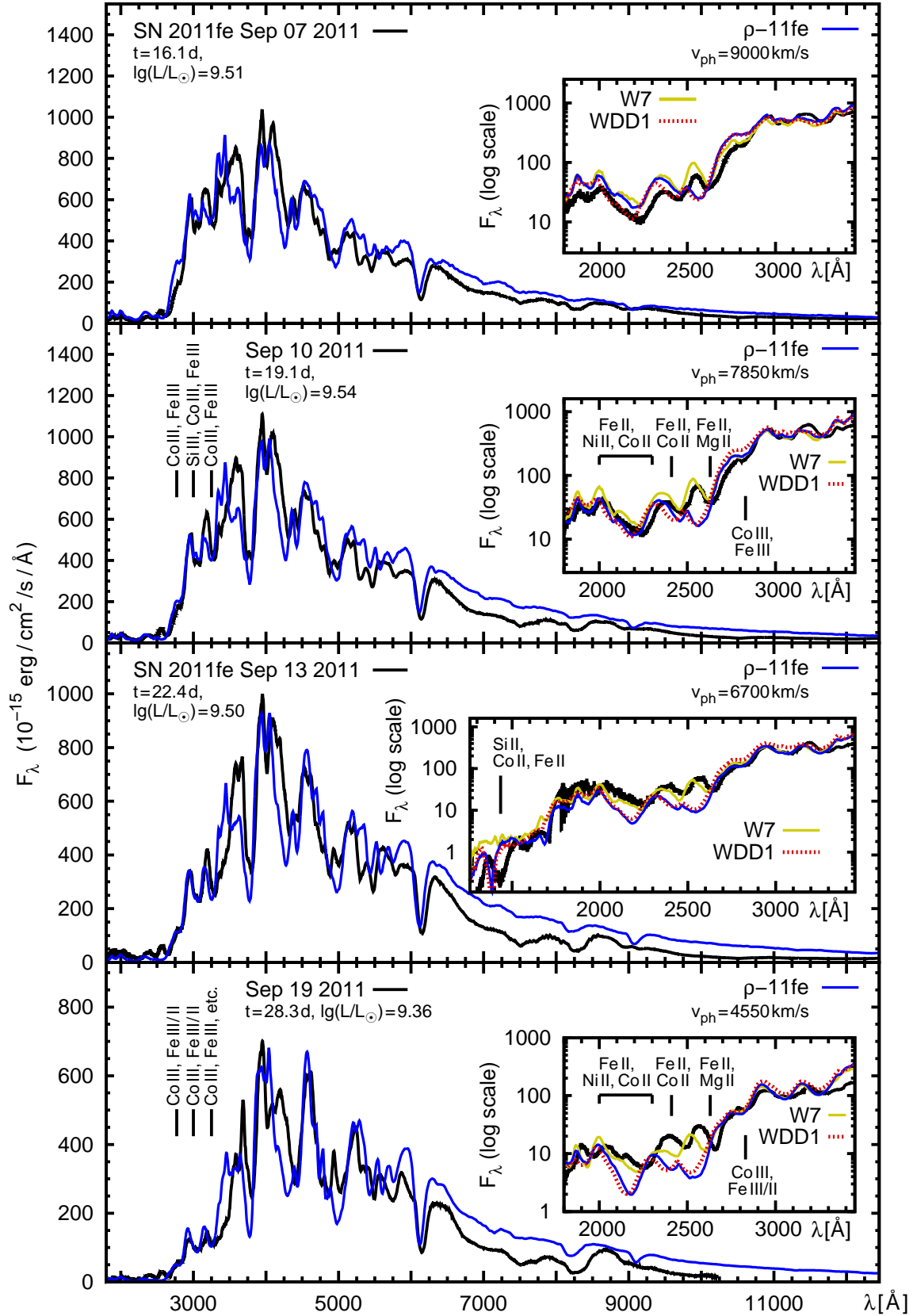
Figure 9. The ρ-11fe model sequence, continued.

model (Iwamoto et al. 1999; Fig. 10, middle panel). 3D delayed-detonation models currently do not seem to agree with similar models in 1D (Seitenzahl et al. 2013).

A thin outer layer above $\sim$19400 km s^{-1} introduced as an extra abundance zone above the August 25 photosphere, containing $\sim$0.01 M$_\odot$, is composed almost exclusively of carbon (98 per cent by mass). A higher oxygen abundance in these layers would lead to spurious absorption in the blue wing of the O I λ7773 feature, as discussed in Section 6.3. We tested the sensitivity of the models to the Fe abundance in the outermost layers, and found that a sub-solar abundance gives the best results (see Sect. 6.1). This is consistent with the metallicity of M101 (Stoll et al. 2011).

The layer immediately below ($16000 < v \leqslant 19400$ km s^{-1}) contains predominantly oxygen (87 per cent by mass). The carbon abundance is low there (2.5 per cent). Some IMEs (e.g. Si, 6 per cent) and even traces of ^{56}Ni (0.1 per cent including decay products ^{56}Co and ^{56}Fe) are also present, as is directly-synthesised Fe (0.2 per cent) and other Fe-group elements. These are required in order to reproduce the observed lines in the August 25 spectrum.

The layer at $13300 < v \leqslant 16000$ km s^{-1} contains a higher fraction of burning products, including Si (20 per cent by mass), directly-synthesised Fe (0.4 per cent), and ^{56}Ni (0.2 per cent).

IMEs dominate the composition at intermediate velocities, between 9000 and 13300 km s^{-1}. The most abundant IME is Si, as expected. Below 9000 km s^{-1}, IMEs decrease, and ^{56}Ni becomes the dominant species. Its abundance reaches $\sim$ 65 per cent below 9000 km s^{-1} and it increases further at lower velocities. The ratio of ^{56}Ni to stable Fe above 11000 km s^{-1} appears to be somewhat higher than in W7 or WDD1. This may be regarded as an indication of a sub-solar metallicity of the progenitor (Iwamoto et al. 1999). Some carbon and oxygen may be present down to 8000 km s^{-1}, with very low abundance (Parrent et al. 2012). The upper limit is set by the strength of the line near 6600 Å and by the appearance of the feature near 7200 Å (Mazzali 2001).

The photosphere of the last spectrum analysed here is at 4550 km s^{-1}. Below this velocity a core of $\sim$ 0.24 M$_\odot$ should exist, which can be analysed by modelling the nebular spectra (e.g. Stehle et al. 2005). Above this velocity we find $\sim$ 0.4 M$_\odot$ of ^{56}Ni in a total mass of $\sim$ 1.14 M$_\odot$. As we cannot establish the exact composition of the core or its mass based on the analysis of photospheric-phase spectra only (see, e.g. , Mazzali et al. 2011; Mazzali & Hachinger 2012), we can only state that our model may contain $0.4-0.7$ M$_\odot$ of ^{56}Ni. This is in good agreement with the W7 and WDD1 models, and with the ^{56}Ni mass estimate from the bolometric luminosity of SN 2011fe (0.53 ± 0.11 M$_\odot$; Pereira et al. 2013). It would not be at all surprising, in fact, if the inner part of the ejecta were dominated by stable Fe-group elements (Höflich et al. 2004; Mazzali et al. 2007). On the other hand, an accurate estimate of the properties of the inner ejecta must await appropriate modelling of the nebular spectra.

6 DISCUSSION

6.1 Fe-group abundances and progenitor metallicity

The distribution of Fe-group elements in SNe Ia largely determines their light curves and greatly affects their spectra. It is therefore a key element when comparing theoretical models to observations (e.g. Mazzali 2000; Mazzali et al. 2001, 2007; Röpke et al. 2007). Different SN Ia explosion models (deflagrations, delayed detonations, double-degenerate mergers) with different progenitor metallicities will differ in their average ^{56}Ni and stable Fe-group yield

and/or in the distribution of these elements. The Fe-group content of SNe Ia with good temporal and spectral coverage can be estimated with high precision (e.g. Stehle et al. 2005; Stritzinger et al. 2006; Tanaka et al. 2011; Hachinger et al. 2013).

Earlier studies suggested that the UV is the spectral region from which the abundance of ^{56}Ni and other Fe-group elements in the outer layers of the SN can best be determined (e.g. Lentz et al. 2000; Walker et al. 2012; Hachinger et al. 2013). Very early light-curve data may also help in this respect (Piro & Nakar 2013b). Foley & Kirshner (2013) derived a sub-solar abundance for the progenitor of SN 2011fe by evaluating models of Lentz et al. (2000) and employing a semi-empirical argument based on the metallicity dependence of the amount of ^{56}Ni versus stable Fe-group elements produced in the explosion. However, this method accounts neither for the different ^{56}Ni production in SNe Ia with different luminosities at fixed progenitor metallicity, nor for the actual Fe-group opacities in SN 2011fe, which can differ from the opacities used by Lentz et al. (2000). With our detailed models for SN 2011fe we can directly investigate the metal content in the outer ejecta, where nucleosynthesis is expected to play a minor role and the progenitor metallicity may still be reflected in the Fe-group content.

We tested the Fe-group content in the outermost layers by recomputing the ρ-11fe-based spectral models and scaling the Fe-group abundances at $v > 19400$ km s^{-1} to different fractions of the solar values (Asplund et al. 2009). Fig. 11 shows that the effect of metallicity is stronger in the UV but more linear in the optical, probably because the latter is less saturated.

The Fe-dominated absorption at $\sim$4800Å in the August 25 spectrum is too strong in the model with solar metallicity (Fig. 11, top panel, inset). This absorption is still present if $Z = 0.1$, but in this case it is practically only caused by Fe located near the photosphere, which is at 13300 km s^{-1}. Si and Mg also contribute significantly, and the shape of the synthetic feature does not match that of the observed one. Actually, this is the only portion of the optical spectrum that is as sensitive to metallicity as the UV, or more. A synthetic spectrum where the Fe-group abundances in the outer layers are set to the metallicity of M101, $Z \simeq 0.5 Z_\odot$, matches the UV-optical spectrum reasonably well. It shows less absorption in the optical Fe feature, which makes it preferable over the $Z_\odot$ model, while the UV flux level does not increase significantly. The model with $Z = 0.3 Z_\odot$ is similarly good. All models show too much flux between 2500 and 3000 Å on Aug 28. This probably reflects remaining shortcomings of ρ-11fe.

In order to test the sensitivity of our models to the assumed parameters, we ran models where we changed the velocity of the photosphere by ± 400 km s^{-1}, a range which represents a realistic uncertainty in this parameter. The change alters the temperature of the lower boundary black-body (deeper photospheres are hotter), but the models yield very similar UV fluxes. This confirms that the flux we see in the UV is not the flux at the lower boundary, but rather radiation re-emitted by metals within the model atmosphere, as already stated by Mazzali (2000).

As a general remark, the sensitivity of the UV spectra to the (virtually) unburned outer layer will crucially depend on that layer's extent. This is evident when comparing the present work with our earlier study of maximum-light spectra (Walker et al. 2012). In those models a larger fraction of the ejecta was considered unburned and tracked the progenitor metallicity. This resulted in a stronger dependence of the spectra on metallicity.

The UV spectra can also be used to diagnose the Fe-group composition in the incompletely burned layers ($\sim 9000 - 13000$ km s^{-1}), where we find mostly ^{56}Ni and
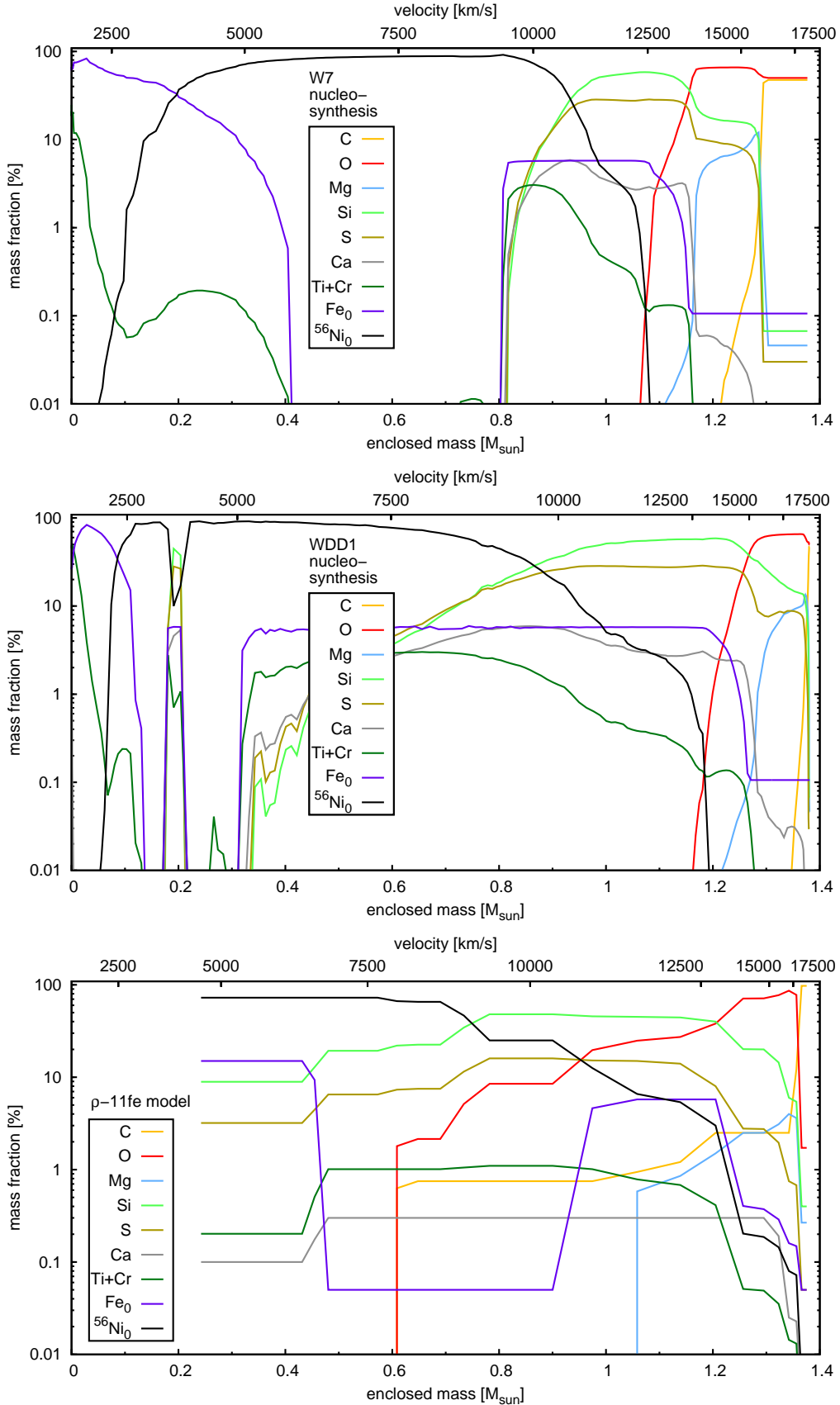
Figure 10. Abundances of W7 and WDD1 nucleosynthesis calculations (Iwamoto et al. 1999, *top and middle panel*, plotted in mass space), compared to our tomography based on ρ-11fe (*lower panel*). The Ni/Co/Fe abundances are given in terms of the mass fractions of ^{56}Ni and stable Fe at $t = 0$ [$X(^{56}$Ni$_0)$, $X($Fe$_0)$]; stable Ni and Co are present only in traces (few per cent or less by mass) in our model.
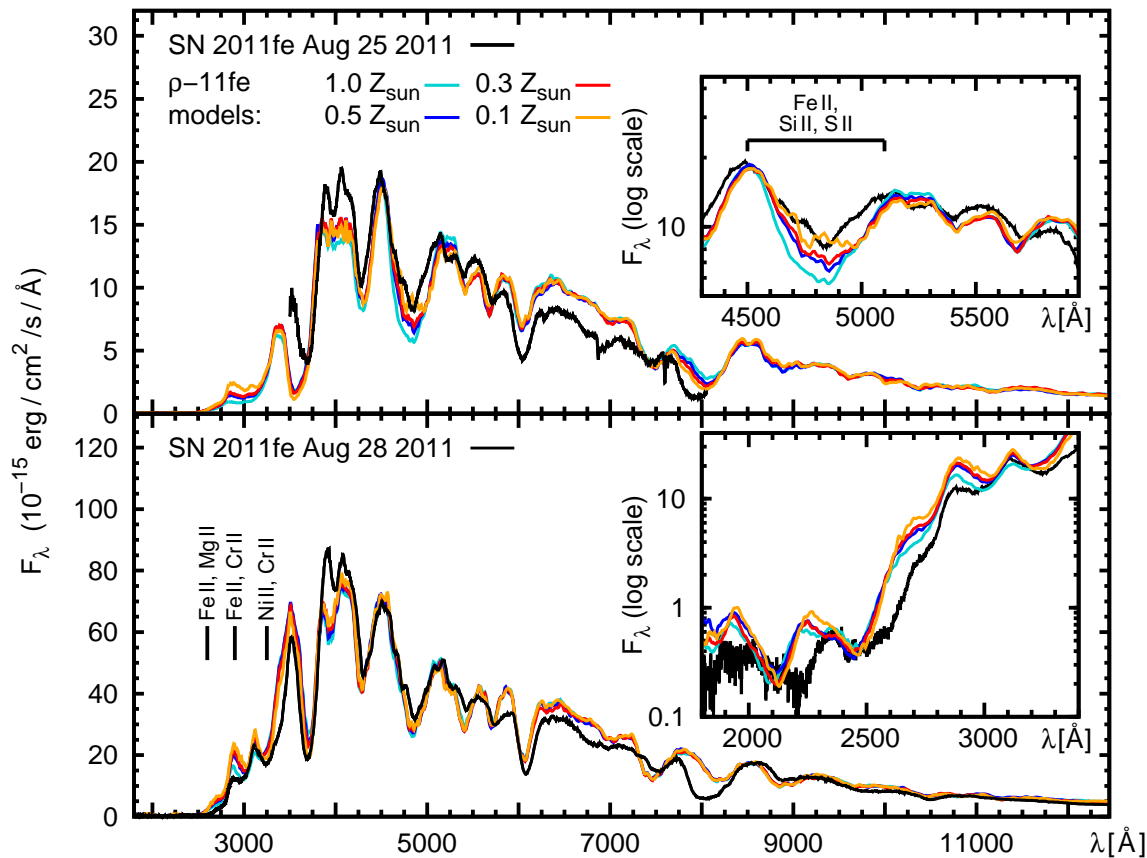
Figure 11. Effect of varying the Fe-group abundances in the outermost layers: earliest spectra of SN 2011fe compared to synthetic spectra from the ρ-11fe model sequence computed for different Fe-group abundances in the outermost layers ($v > 19400\,\mathrm{km\,s^{-1}}$). The insets show the UV in more detail for Aug 28 and the Fe-dominated blend around 4800 Å for Aug 25, respectively.

some directly-synthesised Fe (Section 5.4). This relative composition appears to lie between the solar-metallicity model W7 (where only ^{54}Fe is produced in partially-burned layers because of excess neutrons in ^{22}Ne) and the zero metallicity explosion model 'W70' (Iwamoto et al. 1999), where only ^{56}Ni is produced. This indirectly suggests that the metallicity of the progenitor of SN 2011fe was moderately sub-solar.

6.2 Estimate of rise-time and constraints on the progenitor system

Spectral modelling can be used to estimate the epoch of early spectra through the combined fitting of temperature and line velocity. Our results indicate that the rise-time is larger than estimated by simple analytical fits to the light curve, regardless of the model used. This confirms that diffusion of radiation delays the rise of the light curve. Such a delay was already derived for SN 2010jn (1.0 d; Hachinger et al. 2013). This was a very luminous SN Ia, in which ^{56}Ni was closer to the surface (Hachinger et al. 2013) than in SN 2011fe which was less luminous and declined more rapidly (see also Mazzali et al. 1998; Mazzali et al. 2007, who showed that SNe with a broader distribution of 56Ni as derived from the nebular emission lines also have a broader light curve). The diffusion time of the first photons should therefore be smaller, and the delay smaller. The slightly larger delay in SN 2011fe (1.4 d) is consistent with a smaller ^{56}Ni mass, and with ^{56}Ni being located deeper in the ejecta.

The assumed rise time t_r has implications for the constraints on the progenitor radius determined from the earliest light-curve points. N11 used their first light-curve point (MJD 55797.2) and the earlier non-detections (Section 3.1), together with the analytical early-emission models of Rabinak et al. (2012) and Kasen (2010), to constrain the progenitor radius to $R_{\mathrm{prog}} \lesssim 0.1\,\mathrm{R_\odot}$. Taking into account a later non-detection ($g > 19.0$ at MJD 55796.9), Bloom et al. (2012, hereafter B12) derived $R_{\mathrm{prog}} \lesssim 0.02\,\mathrm{R_\odot}$.

In our ρ-11fe model, the preferred explosion time is 1.4 d earlier than the date inferred by N11, giving an explosion epoch of MJD 55795.3. This makes the limit of $g > 22.2$ (cf. Section 3.1) at MJD 55796.2 the most relevant data point for constraining the progenitor radius. By MJD 55796.2, the SN has had about 22 h for a possible post-shock cooling lightcurve to fade (Piro & Nakar 2013b). Following the analysis of B12 and using the models of Rabinak & Waxman (2011), we derive $R_{\mathrm{prog}} \lesssim 0.02\,\mathrm{R_\odot}$, a very similar constraint to B12. That is, a non-detection of $g > 19.0$ at 4 h after explosion formally gives similar constraints as a non-detection of $g > 22.2$ at 22 h after explosion.

However, as discussed by Rabinak, Livne, & Waxman (2012) and B12, the expressions used for the early SN luminosity from Rabinak & Waxman (2011) assume that the post-shock pressure is dominated by radiation. When the shock diffusion front reaches shells dominated by plasma pressure, a sharp drop in luminosity is expected. The timing of this drop is proportional to the radius of the progenitor (Rabinak et al. 2012), effectively placing an upper limit to this value (B12). At 4 h after explosion this limit is $\lesssim$
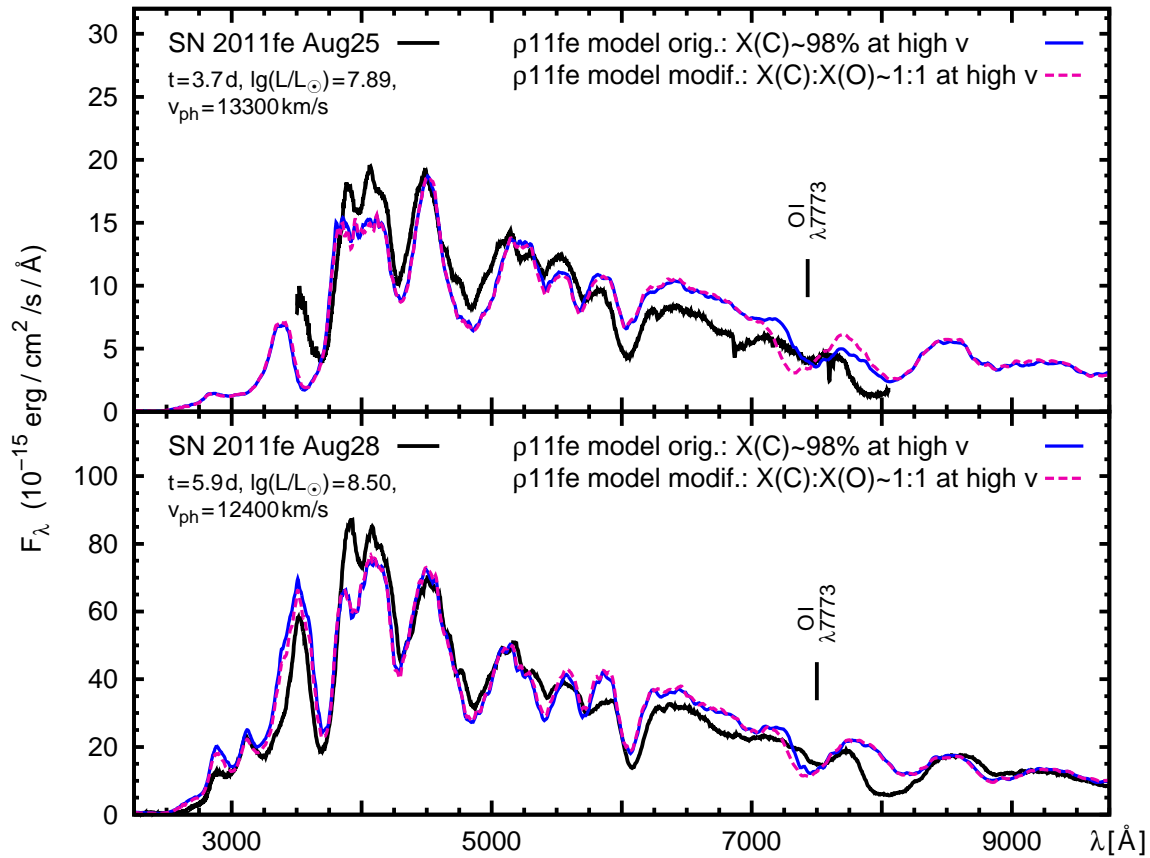
Figure 12. Effect of oxygen in the outermost layers of the model: the earliest two spectra of SN 2011fe (black) compared to ρ-11fe models. A spectrum where the outer layer is almost exclusively composed of carbon (~ 98 per cent by mass, blue/grey, solid lines) fits the observed O I $\lambda7773$ line reasonably well, much better than a model where C and O have the same abundances at $v > 19400 \,\mathrm{km\,s^{-1}}$ (red/grey, dotted lines). In the later spectrum the difference is already much smaller.

$0.02 \,\mathrm{R_\odot}$ (B12), but by 22 h after explosion this rises to $\sim 0.07 \,\mathrm{R_\odot}$. Using the explosion date we estimated, the limits are similar to those of N11, and a factor of a few larger than those of B12.

6.3 Carbon layer

Our models require a carbon-dominated outermost layer, at $v > 19400 \,\mathrm{km\,s^{-1}}$ (Fig. 10). The presence of this layer is supported by the influence carbon has on the spectra: the carbon feature near 6600 Å weakens quickly, which requires carbon to be located at a high velocity. The presence of some heavier elements, consistent with the metal content of the progenitor, is also necessary. On the other hand, oxygen has a negative effect on the spectra: if the outermost layer is assumed to be composed mostly of carbon and oxygen in equal amounts, the O I 7774 Å line is too strong and blue, especially at the earliest epoch modelled (Fig. 12). The O I line in our code matches the observations in a number of different SNe of various types, including SNe Ia at early times, so we see a real difference here. The O abundance may have been too high also in 50:50 carbon-oxygen models for other SNe in the past, but the lack of very early data made this less obvious. This effect decreases with time, which again emphasizes the importance of early data.

This outermost layer should most directly reflect the properties of the accreting material. There may be two scenarios in which an outer carbon-rich layer can develop. The first is via accretion of hydrogen (in a single degenerate system). This hy-

drogen can convert into carbon, but there may be no time for the subsequent conversion into oxygen. A second scenario is via accretion of helium, with the helium then burning to carbon – but this is more unlikely as helium tends to burn explosively to heavier elements. Thus we qualitatively favour the hydrogen-accretion scenario, although data seem to disfavour large companions (Nugent et al. 2011; Bloom et al. 2012; Brown et al. 2012) and a dense CSM (Chomiuk et al. 2012; Margutti et al. 2012) main sequence companions are not ruled out. Detecting this hydrogen, which should be located at high velocities, would be the key to confirming this, but H I lines may require non-thermal excitation (Mazzali et al. 2009; Hachinger et al. 2012), which is not very strong in the first few days after explosion when the optical depth to the γ-rays produced by ^{56}Ni decay deep in the SN is still very large (Mazzali & Lucy 1998). Small amounts of hydrogen (a few $0.01\mathrm{M_\odot}$, Hachinger et al. 2012) may therefore remain undetected. Intriguing indirect evidence for the presence of a small amount of hydrogen comes from the very presence of HVFs, which may be explained as a consequence of the lower ionization regime induced by the presence of some hydrogen and the ensuing contribution to the electron density (Altavilla et al. 2007; Tanaka et al. 2008). In SN 2011fe HVFs are weak, but not absent (see also Parrent et al. 2012). The low upper limit to the mass of H at low velocities deduced qualitatively from nebular spectra by Shappee et al. (2013) appears to be a strong argument against a H-rich companion. This

should be further investigated via detailed nebular modelling of SN 2011fe, which we defer to future work.

7 SUMMARY AND CONCLUSIONS

We have analysed a series of photospheric-epoch UV and optical spectra of the nearby SN Ia SN 2011fe. The spectra can be reproduced using a custom-made density distribution ('ρ-11fe'), which has more material in the outer layers than W7 but does not reach the densities of delayed detonation models. Although this ad-hoc model is characterised by a lower E_K, this value, as well as that of the ejected mass, which is assumed here to be the Chandrasekhar mass, cannot be confirmed until the properties of the inner ejecta are analysed through nebular spectroscopy. The abundance stratification in the outer layers of SN 2011fe is strongly reminiscent of a one-dimensional delayed detonation, but the energy we derived for SN 2011fe is smaller than any published DD model. It would be interesting to verify whether a similar model can be obtained from hydrodymamic calculations. Also, three-dimensional delayed detonation models of non-rotating white dwarfs, which place ^{56}Ni at lower velocities than ^{54}Fe, may be in conflict with the late-time spectra of SNe Ia (Seitenzahl et al. 2013). One alternative possibility is the explosion of a white dwarf with mass slightly lower than the Chandrasekhar value, which could be exploded by the ignition of helium accreting on its surface (Shigeyama et al. 1990; Livne & Arnett 1995; Sim et al. 2010). This may place enough material at high velocities.

Some ^{56}Ni at relatively high velocities is required in order to reproduce the earliest spectra of SN 2011fe. This seems to be a common property of SNe Ia (Mazzali et al. 2008). Stable iron and other Fe-group elements found in the outermost layers, where burning is weak or absent, should be good tracers of the properties of the progenitor. We derive an Fe-group content in these layers consistent with a sub-solar metallicity of the progenitor. The relative Fe-group abundances inferred in the incompletely-burned zones, where stable iron and ^{56}Ni are present in comparable amounts, also seems to point to a sub-solar metallicity (cf. Iwamoto et al. 1999).

Piro & Nakar (2013b) investigated the implications of different ^{56}Ni abundance distributions on the early light curve. In qualitative agreement with their study, we find that the ^{56}Ni distribution in SN 2011fe has a high-velocity tail. However, the abundance of ^{56}Ni in the outermost $0.1 M_\odot$ of the ejecta is very small. This implies that the SN had a 'dark time' between the explosion and the emergence of significant optical light. Spectral analysis is sensitive to the assumed epoch because the density is a function of time. We find that a dark time of $\sim 1.4 \pm 0.5$ d is required. This is somewhat longer than the ~ 0.5 d found by Piro & Nakar (2013b), who assume a higher abundance of ^{56}Ni in the outermost layers. This dark period has implications on the upper limits on the radius of the progenitor ($R_{\rm prog}$) (Nugent et al. 2011; Bloom et al. 2012). We find $R_{\rm prog} \lesssim 0.07\,R_\odot$.

Early UV spectra are an essential tool to explore progenitor metallicities and understand the properties of different SNe Ia. They are much more sentitive to metal content than the optical region. Depending on the distribution of ^{56}Ni and on the presence of other Fe-group elements, the opacity of SNe with similar luminosities can vary (Timmes et al. 2003; Mazzali & Podsiadlowski 2006). This may, for example, explain why SNe with similar luminosity show different evolution of their line velocities (Höflich et al. 2010). It will be important to obtain UV spectral series for other SNe Ia in the future.

This work was made possible by the availability of a high-quality time series of UV-optical spectra. We have inferred explosion properties, including abundances, and crafted a density model that improves the spectra fits, in particular in the UV. This model still has shortcomings, and it is by no means the ultimate solution. However, it demonstrates what can be learned using spectral modelling as a method to investigate all properties of the explosion, not just composition. The availability of an extensive and detailed dataset challenges theoretical models to match the observations. It would be interesting to determine whether a model similar to ours can be obtained from first principles. Cross-fertilisation between observations, modelling and first-principles calculations of stellar evolution and explosion is the only way to make real progress in our physical understanding of SNe Ia.

REFERENCES

Abbott D. C., Lucy L. B., 1985, ApJ, 288, 679
Altavilla G., et al., 2007, A&A, 475, 585
Asplund M., Grevesse N., Sauval A. J., & Scott P. 2009, ARA&A, 47, 481
Astier P., 2012, Rep. Prog. Phys., 75, 116901
Balland C., et al., 2009, A&A, 507, 85
Benetti S., et al., 2005, ApJ, 623, 1011
Bloom J. S., et al., 2012, ApJ, 744, L17
Bosma A., Goss W. M., Allen R. J., 1981, A&A, 93, 106
Branch D., Venkatakrishna K. L., 1986, ApJ, 306, L21
Brown P. J., et al. 2012, ApJ, 753, 22
Bufano F., et al., 2009, ApJ, 700, 1456
Cappellaro E., Turatto M., Fernley J., 1995, ESA-SP 1189
Cardelli J. A., Clayton G. C., Mathis J. S., 1989, ApJ, 345, 245
Chomiuk L., et al. 2012, ApJ, 750, 164
Conley A., et al., 2008, ApJ, 681, 482
Conley A. et al., 2011, ApJS, 192, 1

de Vaucouleurs G., de Vaucouleurs A., Corwin Jr. H. G., Buta R. J., Paturel G., Fouqué P., 1991, Third Reference Catalogue of Bright Galaxies. Vol. III. Spinger, New York, (USA)

Ellis R. S., et al., 2008, ApJ, 674, 51

Foley R. J., Kirshner R. P., 2013, ApJ, 769, L1

Foley R. J. et al., 2008a, ApJ, 684, 68

Foley R. J., Filippenko A. V., Jha S. W., 2008b, ApJ, 686, 117

Foley R. J., et al., 2012a, AJ, 143, 113

Foley R. J., et al., 2012b, ApJ, 753, L5

Foley R. J., et al., 2012c, ApJ, 744, 38

Guy J. et al., 2007, A&A, 466, 11

Hachinger S., Mazzali P. A., Tanaka M., Hillebrandt W., Benetti S., 2008, MNRAS, 389, 1087

Hachinger S., Mazzali P. A., Taubenberger S., Pakmor R., Hillebrandt W., 2009, MNRAS, 399, 1238

Hachinger S., Mazzali P. A., Taubenberger S., Fink M., Pakmor R., Hillebrandt W., Seitenzahl I. R., 2012, MNRAS, 427, 2057

Hachinger S., et al., 2013, MNRAS, 429, 2228

Hayden B. T., et al., 2010, ApJ, 712, 350

Hoeflich P., Wheeler J. C., Thielemann F. K., 1998, ApJ, 495, 617

Höflich P., Gerardy C. L., Nomoto K., Motohara K., Fesen R. A., Maeda K., Ohkubo T., Tominaga N., 2004, ApJ, 617, 1258

Höflich P. et al., 2010, ApJ, 710, 444

Howell D. A., 2011, Nature Communications, 2, 350

Hsiao E. Y. et al., 2013, ApJ, 766, 72

Iwamoto K., Brachwitz F., Nomoto K., Kishimoto N., Umeda H., Hix W. R., Thielemann F., 1999, ApJS, 125, 439

Jeffery D. J., Leibundgut B., Kirshner R. P., Benetti S., Branch D., Sonneborn G., 1992, ApJ, 397, 304

Kasen D., 2010, ApJ, 708, 1025

Kessler R., et al., 2009, ApJS, 185, 32

Khokhlov A. M., 1991, A&A, 245, 114

Kirshner R. P. et al., 1993, ApJ, 415, 589

Law N. M., et al., 2009, PASP, 121, 1395

Leibundgut B., Kirshner R. P., Filippenko A. V., Shields J. C., Foltz C. B., Phillips M. M., Sonneborn G., 1991, ApJ, 371, L23

Lentz E. J., Baron E., Branch D., Hauschildt P. H., Nugent P. E., 2000, ApJ, 530, 966

Livne, E., & Arnett, D. 1995, ApJ, 452, 62

Lucy L. B., 1999, A&A, 345, 211

Maguire K. et al., 2012, MNRAS, 426, 2359

Margutti R., et al. 2012, ApJ, 751, 134

Mazzali P. A., 2000, A&A, 363, 705

Mazzali P. A., 2001, MNRAS, 321, 341

Mazzali P. A., Lucy L. B., 1993, A&A, 279, 447

Mazzali P. A., Lucy L. B., 1998, MNRAS, 295, 428

Mazzali P. A., Schmidt B. P., 2005, in IAU Symposium, Vol. 201, New Cosmological Data and the Values of the Fundamental Parameters, Lasenby A. N., Wilkinson A., eds., p. 241

Mazzali P. A., Podsiadlowski P., 2006, MNRAS, 369, L19

Mazzali P. A., Hachinger S., 2012, MNRAS, 424, 2926

Mazzali P. A., Lucy L. B., Danziger I. J., Gouiffes C., Cappellaro E., Turatto M., 1993, A&A, 269, 423

Mazzali P. A., Cappellaro E., Danziger I. J., Turatto M., & Benetti S. 1998, ApJ, 499, L49

Mazzali P. A., Nomoto K., Cappellaro E., Nakamura T., Umeda H., Iwamoto K., 2001, ApJ, 547, 988

Mazzali P. A., et al., 2005, ApJ, 623, L37

Mazzali P. A., Röpke F. K., Benetti S., Hillebrandt W., 2007, Sci, 315, 825

Mazzali P. A., Deng J., Hamuy M., Nomoto K., 2009, ApJ, 703, 1624

Mazzali P. A., Sauer D. N., Pastorello A., Benetti S., Hillebrandt W., 2008, MNRAS, 386, 1897

Mazzali P. A., Maurer I., Stritzinger M., Taubenberger S., Benetti S., Hachinger S., 2011, MNRAS, 416, 881

Munari U., Henden A., Belligoli R., Castellani F., Cherini G., Righetti G. L., Vagnozzi A., 2013, New Astronomy, 20, 30

Nomoto K., Thielemann F., Yokoi K., 1984, ApJ, 286, 644

Nugent P. E. et al., 2011, Nature, 480, 344

Parrent J. T., et al., 2012, ApJ, 752, L26

Patat F., et al., 2013, A&A, 549, A62

Pereira R., et al., 2013, A&A, 554, A27

Perlmutter S., et al., 1999, ApJ, 517, 565

Piro A. L., Nakar E., 2013a, ApJ, 769, 67

Piro A. L., Nakar E., 2013b, ApJ, submitted (arXiv:1211.6438)

Rabinak I., Waxman E., 2011, ApJ, 728, 63

Rabinak I., Livne E., Waxman E., 2012, ApJ, 757, 35

Rau A., et al., 2009, PASP, 121, 1334

Richmond M. W., Smith H. A., 2012, Journal of the American Association of Variable Star Observers (JAAVSO), 40, 872

Riess A. G., et al., 1998, AJ, 116, 1009

Riess A. G., et al., 2007, ApJ, 659, 98

Röpke F. K., Hillebrandt W., Schmidt W., Niemeyer J. C., Blinnikov S. I., Mazzali P. A., 2007, ApJ, 668, 1132

Röpke F. K. et al., 2012, ApJ, 750, L19

Sauer D. N. et al., 2008a, MNRAS, 391, 1605

Sauer D. N., et al., 2008b, MNRAS, 391, 1605

Schlegel D. J., Finkbeiner D. P., Davis M., 1998, ApJ, 500, 525

Seitenzahl, I. R., Ciaraldi-Schoolmann, F., Röpke, F. K., et al. 2013, MNRAS, 429, 1156

Shappee B. J., Stanek K. Z., 2011, ApJ, 733, 124

Shappee, B. J., Stanek, K. Z., Pogge, R. W., & Garnavich, P. M. 2013, ApJ, 762, L5

Shigeyama, T., Nomoto, K., Tsujimoto, T., & Hashimoto, M.-A. 1990, ApJ, 361, L23

Sim, S. A., Röpke, F. K., Hillebrandt, W., et al. 2010, ApJ, 714, L52

Steele I. A., et al., 2004, in SPIE Conference Series, Oschmann Jr. J. M., ed., Vol. 5489, SPIE, Bellingham WA, p. 679

Stehle M., Mazzali P. A., Benetti S., Hillebrandt W., 2005, MNRAS, 360, 1231

Stoll R., Shappee B., Stanek K. Z., 2011, ATEL 3588

Stritzinger M., Mazzali P. A., Sollerman J., Benetti S., 2006, A&A, 460, 793

Sullivan M., et al., 2011, ApJ, 737, 102

Suzuki N., et al., 2012, ApJ, 746, 85

Tanaka M., Mazzali P. A., Maeda K., Nomoto K., 2006, ApJ, 645, 470

Tanaka M., et al., 2008, ApJ, 677, 448

Tanaka M., Mazzali P. A., Stanishev V., Maurer I., Kerzendorf W. E., Nomoto K., 2011, MNRAS, 410, 1725

Timmes F. X., Brown E. F., Truran J. W., 2003, ApJ, 590, L83

Vinkó J., et al., 2012, A&A, 546, A12

Walker E., et al., 2012, MNRAS, 427, 103

Wang X., et al., 2012, ApJ, 749, 126

Yaron O., Gal-Yam A., 2012, PASP, 124, 668